SDR Implemented Ground-based Interferometric Radar for Displacement Measurement

Weike Feng *Member, IEEE,* Jean-Michel Friedt, Pengcheng Wan

***Abstract*—We demonstrate in this paper the use of general Software Defined Radio (SDR) hardware for ground-based interferometric radar (GBIR) system development for static target imaging and displacement estimation purposes. Firstly, a system synchronization approach is proposed within the free and open-source framework GNU Radio, followed by a frequency-domain bandwidth synthesis method used to improve the range resolution with three different waveforms. Secondly, data preprocessing and target imaging methods are proposed to reduce the negative influences of practical non-ideal factors and to get high-quality target images. Last, various experiments are conducted to show the performance of the developed SDR-GBIR system and the proposed methods. It is shown that high-resolution target image and high-accuracy displacement measurement can be obtained by our SDR-GBIR systems.**

***Index Terms*—Software defined radio, Ground-based interferometric radar, Radar imaging, Displacement measurement.**

I. Introduction

Over the last two decades, ground-based interferometric radar (GBIR) has been extensively applied for contact-less, real-time, continuous, high-resolution, and high-accuracy displacement measurements of geophysical (landslide or volcano) and man-made (bridge or dam) structures [1]–[4]. Compared with conventional displacement measurement methods, such as geodetic and laser scanning methods [5], from a single position (maybe outside from the Area of Interest – AoI), GBIR can observe a longer distance, has a larger space coverage, and is able to work days-and-nights in all weather conditions. Compared with space-borne interferometric radar [6], [7], its higher data sampling rate and higher spatial resolution make GBIR preferable for real-time displacement monitoring of a local area. Besides, without of orbit limitation, GBIR can be installed at almost any selected position to have an optimal observation angle to extract useful displacement information of the illuminating scene.

For GBIR, imaging resolutions in range, azimuth, and elevation directions are important to distinguish different targets in the AoI with potential displacements. In order to obtain high range resolution, the simple approach is to increase the bandwidth of the transmitted signal, and, to achieve high cross-range resolutions, synthetic aperture radar (SAR) technique [8] or multiple-input-multiple-output (MIMO) radar technique [9] is normally used, resulting in various GB-SAR and GB-MIMO radar systems. Representatives of GB-SAR systems are [10]–[14]: LISA system from Joint Research Centre (JRC) of the European Commission, IBIS system from IDS GeoRadar company, Fast-GBSAR system from MetaSensing company, GB-NWSAR system from Institute for radiophysics and electronics, and Arc-SAR system from Chinese Academy of Sciences. On the other hand, representatives of GB-MIMO radar systems are [15]–[19]: Melissa system from JRC of the European Commission, MIMO-SAR system from Beijing Institute of Technology, SPARX system from IDS GeoRadar company, compressive sensing (CS) based MIMO radar system from University of Florence, and cross-MIMO radar system from Tohoku University.

Although the theoretical research and practical applications of GB-SAR and GB-MIMO radar are fruitful, some limitations exist. On the one hand, exiting GB-SAR and GB-MIMO radar systems are highly specialized and integrated, developed for specific tasks. The lack of universality and openness of software and hardware modules makes their construction and maintenance cost high. On the other hand, the parameters of most GB-SAR and GB-MIMO radar systems are difficult to change to adapt to the environment, i.e., the system cannot be easily reconfigured for different applications (for example, the waveform type is fixed and the working frequency is usually in a fixed band). In such a case, the signal processing platform can only passively process the received signal, without the capability to adjust the system parameters in real time according to the obtained results in previous measurements, as needed by cognitive radar [20], [21], the future of modern radar systems. In other word, current GB-SAR and GB-MIMO radar systems have the problem of poor flexibility.

Recently, Software Defined Radar (SDRadar) systems [22]–[24] have been developed to use the Software Defined Radio (SDR) hardware for radar applications, showing the potentials to solve the problems of the complicated, expensive, and non-reconfigurable conventional radar. For different applications, SDRadar only needs to redefine the hardware functions through software programming without the need to change actual hardware device, hence characterized by universality and reconfigurability. Therefore, to reduce the development cost and improve the system flexibility, we demonstrate the use of SDR to implement GBIR systems for displacement estimation in this paper, including an SDR-GB-SAR system to obtain 2D target image and an SDR-GB-MIMO radar system to obtain 3D target image, with different types of commonly used waveforms for displacement measurement by GBIR [1]: stepped frequency continuous waveform (SFCW), frequency-modulated continuous waveform (FMCW), and noise waveform (NW). Different from previous approaches [23], [24], this work focuses exclusively on SDRadar running on general

W. F and P. W are with Air Force Engineering University, Xian, China. J.-M. Friedt is an associate professor at Franche-Comté University with his research activities hosted by the Time & Frequency department of the FEMTO-ST Institute in Besançon, France. E-mail: jmfriedt@femto-st.fr.

purpose central processing unit (CPU) within the free and open-source SDR framework GNU Radio, and does no rely on modifying the Field Programmable Gate Array (FPGA) bitstream for generating and collecting signals, hence lowering the technical requirements for system development.

Four challenges to realize SDR-GBIR we address in this paper are: 1) synchronization of transmitter and receiver without FPGA programming but keeping the original SDR firmware, 2) using commercial off the shelf (COTS) general SDR hardware to get high range resolution, 3) preprocessing the measured data to reduce the negative influences caused by practical non-ideal factors, and 4) advanced signal processing to obtain high-quality 2D and 3D target image. Specifically, 1) a dual-channel receiver sampling simultaneously the reference signal coupled from the transmitter and the measurement signal collected by the receiving antenna has been applied to system synchronization, 2) the frequency-domain bandwidth synthesis approach has been used to obtain high range resolution with three different waveforms, 3) delay-amplitude calibration and least-squares (LS) based direct-path interference (DPI) suppression [25], [26] have been conducted to improve the system performance, and 4) a novel CS based method have been proposed to improve the imaging quality of SDR-GB-SAR and SDR-GB-MIMO radar systems.

The remainder of this paper is organized as follows. In Section II, the overview of the designed SDR-GBIR system is given, including its structure and working flow, transmitting & receiving (TR) subsystem, and controlling & date acquisition (CDA) subsystem. In Section III, the signal model of the SDR-GBIR system is established, which facilitates the description of the Signal Processing (SP) subsystem. In Section IV, the main signal processing steps, e.g., system synchronization, bandwidth synthesis, data preprocessing, high-resolution imaging, and displacement estimation by interferometric process, are introduced. Then, in Section V, experiment results are presented to demonstrate the performance of the developed SDR-GBIR systems in practice, together with the displacement estimation accuracy analysis considering atmospheric conditions and the implementation of SDR-GBIR system with orthogonal frequency division multiplexing (OFDM) Wireless Fidelity (Wi-Fi) signal. Finally, section VI concludes this paper.

II. System overview

In this Section, we overview the design method of the SDR-GBIR system, whose general structure is shown in Fig. 1, demonstrating its basic principle and main subsystems. As we can see from Fig. 1, the overall working flow of SDR-GBIR can be expressed as follows:

1) Based on a TCP/IP server written as a Python Module in GNU Radio, the control software (in a personal computer or an embedded single board computer Raspberry Pi 4 (RPi 4)) sends commands to GNU Radio through a TCP/IP client;
2) GNU Radio generates and inputs a baseband signal with specific waveform type and parameters to the transmitting unit;
3) After digital to analog conversion (DAC), frequency mixing for up-conversion, power amplifying, and filtering, the RF signal is radiated out by a fixed transmitting antenna in the SDR-GB-SAR case or a selected transmitting antenna in the SDR-GB-MIMO radar case, as well as be coupled to the receiving unit as a reference signal.
4) The receiving unit receives two channels of signals, one being the reference signal from the transmitting unit and the other being the measurement signal collected by a moving or selected receiving antenna;
5) Through filter, low-noise-amplifier, frequency mixer for down-conversion, and analog to digital converter (ADC), the two channels of signals are sampled, interleaved, and transfered continuously by a non-blocking ZeroMQ publish socket;
6) The control software fetches the data through a ZeroMQ subscribe socket and sends it to the SP subsystem;
7) Repeat steps 1 to 6 for bandwidth synthesis and antenna moving (or antenna selection);
8) The SP subsystem processes all the received data to obtain target imaging and displacement measurement results and adjusts system parameters accordingly for the following measurements, if needed, by sending commands to the control software.

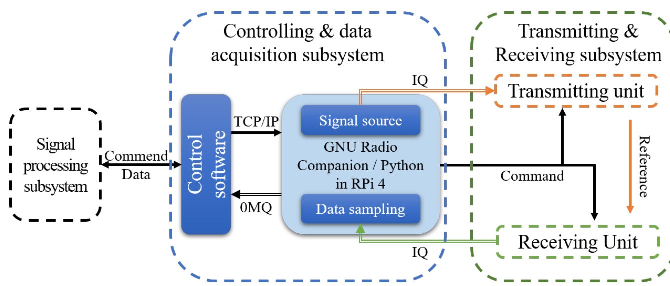

Fig. 1. The general structure of SDR-GBIR with three main subsystems: transmitting & receiving subsystem, controlling & data acquisition subsystem, and signal processing subsystem.

In the following, the functions and components of TR and CDA subsystems will be explained with specific focuses on system synchronization, signal source generation, parameter changing and data acquisition, leaving the details of the SP subsystem and its related signal processing methods in Section IV.

A. Transmitting & receiving subsystem

The first core challenge met by SDRadar implementation is synchronization of the transmitter and the receiver, as general purpose SDR is unable to synchronize emission and reception within sub-microsecond (150 m two-way trip). While the classical approach for synchronization is to modify the FPGA firmware to achieve controlled latency between emission and reception [24], it limits the flexibility of the software approach since the FPGA must be reconfigured for each new emitted sequence. Therefore, we proposed an approach by separating transmitting and receiving hardware to ease synchronization issues, as shown in Fig. 2, where a PlutoSDR module from

Analog Devices is used as the single-channel transmitter and a USRP B210 from Ettus Research is used as the coherent dual-channel receiver, with one channel (called as reference channel) recording the transmitted signal and the second channel (called as measurement channel) recording the signal collected by the receiving antenna. Under such a scheme, the synchronization between the transmitter and receiver can be obtained for all the generated waveforms, i.e., SFCW, FMCW, and NW, by simple coherent processing methods, as will be explained in Section IV. The flexibility of this approach is emphasized by replacing the PlutoSDR with a Wi-Fi emitter, proving a covert solution best suited to urban environment monitoring as well as complementing radar application with digital communication, as will be shown in Section V.

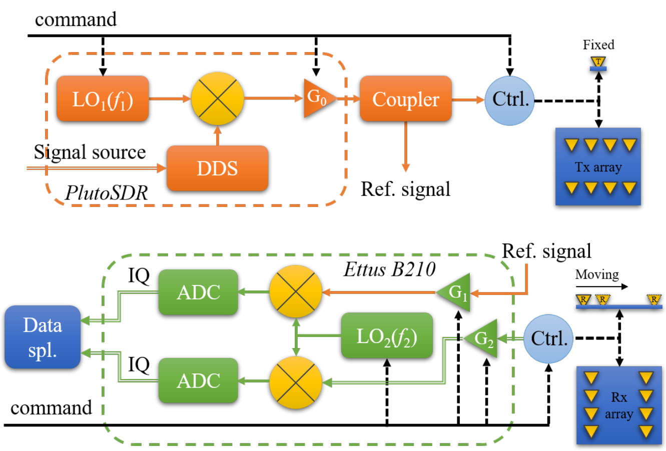

Fig. 2. The transmitting & receiving subsystem of SDR-GBIR: the top sub-figure shows the transmitting unit and the bottom sub-figure shows the receiving unit. DDS refers to Direct Digital Synthesis of the radiofrequency local oscillators LO. The "Ctrl" blocks refer either to antenna moving control or antenna switching control circuitry.

Besides, as shown in Fig. 2, in addition to the single-channel transmitter PlutoSDR and the dual-channel receiver B210, the TR subsystem also includes a transmitting antenna (array) and a receiving antenna (array). In the case of SDR-GB-SAR, a receiving patch antenna is scanning uniformly along a linear rail connected to a micro-controller to achieve the azimuth resolution with a transmitting patch antenna at a fixed location. As to SDR-GB-MIMO radar, small-size, high-gain, and ultra-wideband Vivaldi antennas with the double-slot structure [27] are used to generate the 2D transmitting and receiving arrays, whose corresponding virtual array is a uniform planar array (UPA), to get the azimuth and elevation resolutions. Moreover, for SDR-GB-MIMO radar, two 1×8 switches are added to realize the time-divided signal transmitting and receiving. Here, we note that, since the SDR transmitter/receiver is fitted with only one/two channel(s), the SDR-GB-MIMO structure results from multiplexing the transmitting and receiving channels, with each individual measurement being actually SISO (Single Input Single Output), and a MIMO array will be finally constructed by switching all antennas in the transmitting and receiving arrays.

B. Controlling & data acquisition subsystem

The CDA subsystem is the main part of software programming for the SDR-GBIR system, which is realized based on an external control software and a single board computer RPi 4, as shown in Fig. 3. Our implementation of the external control software in this paper is with GNU/Octave and its `zeromq` & `socket` toolboxes since digital signal processing can be easily implemented in this framework in a personal computer, although all functions can be ported to Python in order to achieve a fully autonomous implementation running on RPi 4. The consistent embedded GNU/Linux generation framework Buildroot was used in order to provide efficient cross-compilation toolchain, Linux kernel, bootloader, and userspace libraries and applications tuned to the RPi 4 processor characteristics, including GNU Radio Companion, `libuhd` the Universal Hardware Driver for Ettus Research platforms supporting the dual-channel receiver B210 connected to the USB-3 communication bus, `gr-iio` and `libiio` Analog Device's Industrial Input/Output libraries and GNU Radio interface for controlling their hardware for sending data to the transmitter PlutoSDR connected to the USB-2 communication bus, and `numpy` for signal processing with Python3. Such an optimized, custom toolchain is mandatory to achieve best performances of the embedded board which would not be efficiently used with a general purpose, binary distribution [28]: this work contributes by having ported the GNU Radio tools and associated libraries as part of the standard Buildroot packages.

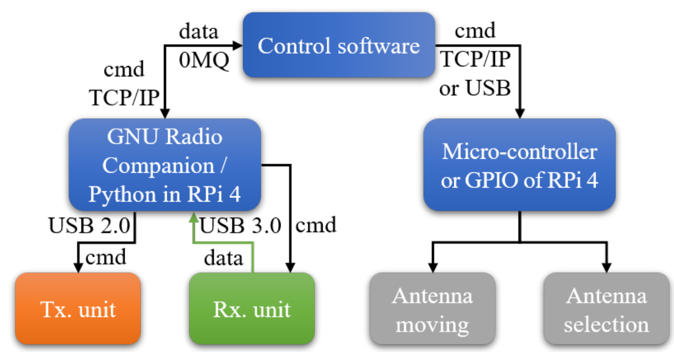

Fig. 3. The controlling & data acquisition subsystem of SDR-GBIR used to control the transmitting parameters, receiving parameters, and antenna moving (or selection), and to send data to and receive commands from the SP subsystem.

(1) Signal source generation and bandwidth synthesis

The second core challenge met by the implementation of SDRadar, beyond the system synchronization, is to achieve a wide enough bandwidth to reach a targeted range resolution. However, general SDR hardware (i.e., PlutoSDR and B210) is plagued with the bandwidth limited by the ADC and DAC loss of resolution with increasing sampling rate, as well as the communication bandwidth between SDR and the data acquisition platform (RPi 4), resulting in a poor range resolution. For example, a 2-MHz bandwidth, as provided by the USB-2 communication when sending the baseband signal to PlutoSDR, will only allow for a 75 m range resolution, while, for GBIR displacement estimation, the needed range resolution is normally in meter or sub-meter level [1]. We have observed that no radiofrequency sample was lost when communicating with the PlutoSDR over the USB-2 bus at a maximal sampling rate of 2.7 MS/s, and this sampling rate was hence selected throughout the experiments.

A natural solution to get a wide bandwidth for SDRadar is using the bandwidth synthesis approach [29], a technique also known as frequency stacking [24], and its simplest way is to transmit a single-frequency continuous waveform in each TR routine and increase its carrier frequency step by step until a desired bandwidth, which eventually forms the SFCW signal. However, for SFCW signal, the maximal detection range is limited by the frequency step. In order to have a larger detection range while keeping the same range resolution, the frequency step should be reduced and thus the number of frequencies should be increased, resulting in a longer measurement duration. To solve this problem, either the frequency-modulated approach or the phase-coded approach [30], [31] can be applied to each TR routine to fully use the limited bandwidth of SDR. Here, we note that, to make it consistent with the common GBIR statements, we refer the transmitting signals based the frequency-modulated approach and the bi-phase-coded approach with a pseudo-random noise sequence in each TR routine to FMCW and NW, respectively.

In actual SDR-GBIR implementation, we can generate a constant source input, use a Voltage Controlled Oscillator (VCO) block to generate a linearly frequency modulated signal input, and use a Random Source block to generate a pseudo-random bi-phase-coded noise signal input, from GNU Radio, to PlutoSDR for SFCW, FMCW, and NW signal transmitting. Then, by simultaneously sweeping the local oscillator frequencies of PlutoSDR and B210, we do bandwidth synthesis and obtain the desired range resolution. While the default configuration of PlutoSDR is to fully reconfigure the AD9363 radio-frequency front-end with multiple calibration steps requiring up to 1 s to stabilize, custom software was back-ported in the gr-iio library to only reconfigure the local oscillator [32]. Thanks to this configuration, negligible settling time is observed after tuning the PlutoSDR local oscillator. The approach to properly change the local oscillator frequency will be detailed in the following.

(2) Parameter changing and data acquisition

Since the local oscillators of both the transmitter and receiver should be adjusted simultaneously and only when stabilized can relevant data be collected, advanced parameter changing and data acquisition approach should be used as GNU Radio does not allow for discontinuous data-streams to be recorded. The proposed approach, as shown in Fig. 4, is to use a TCP server running in the GNU Radio flowchart to change the local oscillator frequencies under external controlling commands, and to stream collected data to the external control software through a non-blocking UDP-like socket implemented as a ZeroMQ publish socket, as detailed as follows.

Rather than modifying the Python code generated by GNU Radio, which prevents returning to the graphical user interface once the Python code has been appended with new functionalities, we use the Python Module to add our custom code-namely a separate thread running a TCP server that is able to access the methods provided by the calling program – and execute this thread from the main program by appending the initialization function with the thread call. Calling the thread with the `self` argument allows to modify asynchronously the flow-graph properties and the variables defining the system parameters (e.g., local oscillator frequencies, data sampling rate and duration, signal source type and parameters, TR gains and filtering parameters).

Having found the ability to change the system parameters during a measurement, we should save data when acquisition conditions are stable. Because the continuous data-stream includes the state transition as the hardware properties are modified, the external software controlling the hardware can also synchronize acquisition by fetching the broadcast data only when the hardware is known to be in a stable condition. Rather than using the UDP Sink from GNU Radio, we have selected to use the higher level ZeroMQ framework and its equivalent Publish server. A Subscribe client connects to this server whenever the data-stream is expected to be stable following hardware reconfiguration, and data are otherwise lost if no listening socket has been connected to the server. Since ZeroMQ has been ported to multiple languages, all are suitable for running the client, we have selected GNU/Octave (running on a personal computer) or Python (running on RPi 4 for a fully autonomous implementation) for fetching data. Notice that the flowchart in Fig. 4 does not involve any graphical user interaction and hence is well suited to run on the embedded board, even if lacking a frame buffer or other graphical interfaces.

At last, as shown in Fig. 3, the CDA subsystem also has the functions of moving the receiving antenna on a rail for the SDR-GB-SAR case and selecting the TR antennas for the SDR-GB-MIMO radar case. In the former case, this is achieved by setting the receiving antenna on a motorized rail driven by a lead-screw setup using a stepper motor, controlled by a dedicated micro-controller receiving the commands through its USB (virtual serial) port from the external software controller. In the later case, the two 1×8 switches are connected to the GPIO interface of RPi 4 with a 74LS373 chip as the address latching unit. By changing the voltage levels of the GPIO interface according to the commands from the external software controller, the function of antenna selection is realized.

III. Signal Model

In this Section, considering practical non-ideal factors, i.e., the DPI caused by the mutual coupling between transmitting antenna and receiving antenna as well as the delay-amplitude differences among different measurement channels, we establish the signal model for the developed SDR-GBIR system.

Firstly, assuming the transmitting antenna is at its i-th position and the receiving antenna is at its j-th position, the transmitted signal in the q-th TR routine is modeled as

$$s^{i,j,q}(t) = s_0(t)e^{j(2\pi f_{lo}^{1,q}t+\psi_0^{i,j,q})} \tag{1}$$

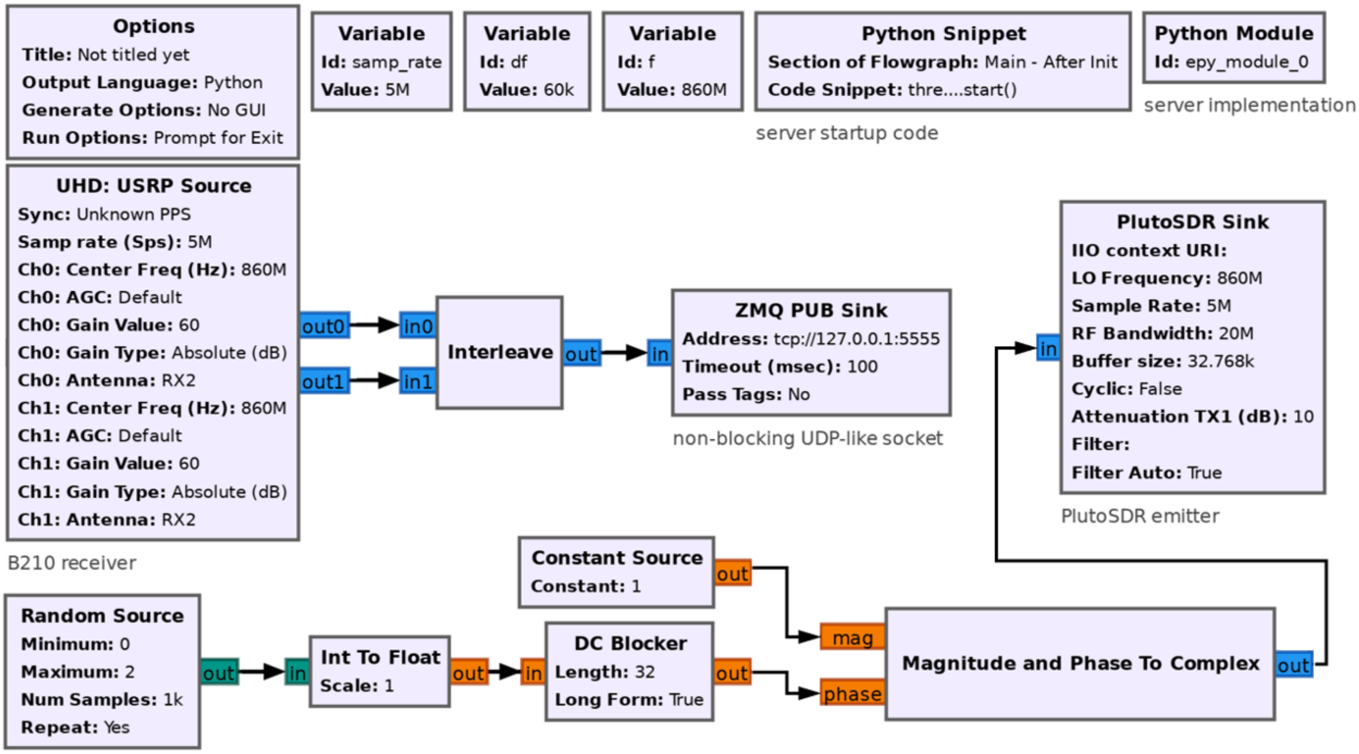

Fig. 4. Demonstration of the inclusion of a TCP server in the Python Module as part of a GNU Radio flow-graph for parameter changing and a non-blocking ZeroMQ publish socket for data acquisition.

where $i = 1, 2, ..., I$ (I is the number of transmitting position and equals to 1 for SDR-GB-SAR) , $j = 1, 2, ..., J$ (J is the number of receiving position), $q = 1, 2, ..., Q$ (Q is the number of carrier frequencies), $f_{lo}^{1,q}$ denotes the q-th local oscillator frequency of the transmitter, $\psi_0^{i,j,q}$ denotes the initial phase, $s_0(t)$ denotes the baseband signal, and t denotes time with a sampling interval of ΔT and a duration of T.

In Eq. (1), the signal amplitude is assumed to be constantly one without loss of generality, and the baseband signal can be expressed as $s_0(t) = 1$ for SFCW, $s_0(t) = e^{-j\pi\gamma(t-T/2)^2}$ with γ as the chirp rate for FMCW, or $s_0(t) = \sum_{k=1}^{K} b_k(t)e^{-j\psi_k}$ for NW, where

$$b_k(t) = \begin{cases} 1, & (k-1)\tau_c \le t \le k\tau_c \\ 0, & \text{otherwise} \end{cases} \tag{2}$$

with $k = 1, 2, ..., K$, K as the code length, $\tau_c = T/K$ as the chip interval, and ψ_k as the k-th phase value that offsets the relative carrier phase during τ_c [31]. Under the bi-phase coding scheme used in this paper, ψ_k is either 0 or π according to a pseudo-random noise sequence.

Then, the simultaneously sampled reference and measurement signals can be expressed by

$$\begin{cases} s_r^{i,j,q}(t) = s_0(t-\tau_{ref})e^{j2\pi[\Delta f_{lo}^q t - f_{lo}^{1,q}\tau_{ref}]+j\psi_0^{i,j,q}} \\ s_m^{i,j,q}(t) = s_{m,D}^{i,j,q}(t) + s_{m,T}^{i,j,q}(t) + s_{m,E}^{i,j,q}(t) \end{cases} \tag{3}$$

where $\Delta f_{lo}^q = f_{lo}^{1,q} - f_{lo}^{2,q}$ denotes the local frequency difference between the transmitter and receiver, $f_{lo}^{2,q}$ denote the q-th local oscillator frequency of the receiver, τ_{ref} denotes the constant delay of the reference channel,

$$s_{m,D}^{i,j,q}(t) = \sigma_D^{i,j,q} s_0(t-\tau_D^{i,j})e^{j2\pi[\Delta f_{lo}^q t - f_{lo}^{1,q}\tau_D^{i,j}]+j\psi_0^{i,j,q}} \tag{4}$$

denotes the DPI component in the measurement channel with $\tau_D^{i,j}$ and $\sigma_D^{i,j,q}$ as its delay and complex amplitude,

$$s_{m,T}^{i,j,q}(t) = \sum_{n=1}^{N} \sigma_n^{i,j,q} s_0(t-\tau_n^{i,j})e^{j2\pi[\Delta f_{lo}^q t - f_{lo}^{1,q}\tau_n^{i,j}]+j\varphi_0^{i,j,q}} \tag{5}$$

denotes the target component in the measurement channel with $\tau_n^{i,j}$ and $\sigma_n^{i,j,q}$ as the delay and complex amplitude of the n-th target component ($n = 1, 2, ..., N$ and N is the number of targets), and $s_{m,E}^{i,j,q}(t)$ denotes the noise component, which is ignored in the following to facilitate the derivations.

The delays and complex amplitudes of the DPI component and the n-th target component can be expressed as

$$\begin{cases} \tau_D^{i,j} = \tau_{meas}^{i,j} + \tau_{D,0}^{i,j}, & \tau_n^{i,j} = \tau_{meas}^{i,j} + \tau_{n,0}^{i,j} \\ \sigma_D^{i,j,q} = \sigma_{meas}^{i,j,q}\sigma_{D,0}^{i,j}, & \sigma_n^{i,j,q} = \sigma_{meas}^{i,j,q}\sigma_n^0 \end{cases} \tag{6}$$

where $\tau_{meas}^{i,j}$ and $\sigma_{meas}^{i,j,q}$ denote the intrinsic delay and complex amplitude of the measurement channel caused by the connection cables and other factors (in the SDR-GB-SAR case, they are not dependent on i and j, while, in the SDR-GB-MIMO radar case, they are), $\tau_{D,0}^{i,j}$ and $\tau_{n,0}^{i,j}$ denote the delays of the DPI and the n-the target, $\sigma_{D,0}^{i,j}$ and σ_n^0 denote the complex amplitudes of the DPI and the n-the target.

We note that, in Eqs. (3) and (6), we use the following assumptions without loss of generality: 1) the amplitude of the reference channel is constantly one, i.e., $\sigma_{ref} = 1$; 2) the delays are not related to the frequency; 3) the amplitude of the DPI is not related to the frequency but related to the antenna position; 4) the amplitude of the target is neither related to the frequency nor related to the antenna position as the targets are normally at the far range; and 5) the intrinsic amplitude of the measurement channel is set to be dependent on the frequency to be more consistent with the practice. Besides, as the isolation between the reference and measurement channels of the B210 is measured at about 75 dB at 600 MHz, 70 dB at 1000 MHz, 60 dB at 2400 MHz, and 58 dB at 5800 MHz, no interference between the reference channel and measurement channel is considered.

At last, since most signal processing steps are conducted in the frequency-domain in this study, we obtain the spectra of the reference and measurement signals as

$$\left\{ \begin{array}{c} S_r^{i,j,q}(f) = S_0(f-\Delta f_{lo}^q)e^{j\psi_0^{i,j,q}}e^{-j2\pi(f+f_{lo}^{2,q})\tau_{ref}} \\ S_m^{i,j,q}(f) = S_{m,D}^{i,j,q}(f) + \sum\limits_{n=1}^{N} S_{m,n}^{i,j,q}(f) \end{array} \right. \tag{7}$$

where f denotes frequency, $S_0(f)$ denotes the spectrum of the baseband signal, and

$$\left\{ \begin{array}{l} S_{m,D}^{i,j,q}(f) = S_0(f-\Delta f_{lo}^q)e^{j\psi_0^{i,j,q}}\sigma_D^{i,j,q}e^{-j2\pi(f+f_{lo}^{2,q})\tau_D^{i,j}} \\ S_{m,n}^{i,j,q}(f) = S_0(f-\Delta f_{lo}^q)e^{j\psi_0^{i,j,q}}\sigma_n^{i,j,q}e^{-j2\pi(f+f_{lo}^{2,q})\tau_n^{i,j}} \end{array} \right. \tag{8}$$

IV. Signal processing

In this Section, we introduce the details of the SP subsystem, i.e., we present the signal processing methods of SDR-GBIR to get high-resolution and high-quality target imaging and displacement estimation results, including system synchronization, bandwidth synthesis, data preprocessing, high-resolution imaging, and interferometric process.

A. System synchronization

As mentioned in Section II-A, the synchronization of the SDR-GBIR system can be obtained by simple coherent processing, which is explained here in detail.

Given Eq. (7), either by matched filtering or inverse filtering [33], the reference and measurement signals can be combined to give the following complex frequency-domain signal

$$\begin{aligned} S^{i,j,q}(f) &= S_m^{i,j,q}(f)[S_r^{i,j,q}(f)]^* \\ &= |S_0(f-\Delta f_{lo}^q)|^2[\sigma_D^{i,j,q}e^{-j2\pi(f+f_{lo}^{2,q})(\tau_D^{i,j}-\tau_{ref})} \\ &+ \sum_{n=1}^{N}\sigma_n^{i,j,q}e^{-j2\pi(f+f_{lo}^{2,q})(\tau_n^{i,j}-\tau_{ref})}] \end{aligned} \tag{9}$$

with $[\cdot]^*$ as the complex conjugate or

$$\begin{aligned} S^{i,j,q}(f) &= S_m^{i,j,q}(f)/S_r^{i,j,q}(f) \\ &= \mathrm{Rect}\left(\frac{f-\Delta f_{lo}^q}{B_0}\right)[\sigma_D^{i,j,q}e^{-j2\pi(f+f_{lo}^{2,q})(\tau_D^{i,j}-\tau_{ref})} \\ &+ \sum_{n=1}^{N}\sigma_n^{i,j,q}e^{-j2\pi(f+f_{lo}^{2,q})(\tau_n^{i,j}-\tau_{ref})}] \end{aligned} \tag{10}$$

with $\mathrm{Rect}\,(x) = \left\{ \begin{array}{ll} 1, & -1/2 \le x \le 1/2 \\ 0, & \text{otherwise} \end{array} \right.$ and B_0 as the bandwidth of the baseband signal.

It should be noted that, based on either Eq. (9) or Eq. (10), system synchronization can be realized. However, in the former case, the square of spectrum magnitude magnifies any divergence from the flat spectrum, while, in the latter case, such magnitude fluctuation is canceled. Therefore, with a pure reference signal to minimize the signal to noise ratio (SNR) loss of the inverse filtering method [33], we use Eq. (10) in this study.

It can be seen from Eq. (10) that, by selecting $S_u^{i,j,q}(f)$ from $S^{i,j,q}(f)$ with the frequencies satisfying $-B_u/2 \le f_u \le B_u/2$ (where B_u denotes the usable bandwidth determined by the signal bandwidth B_0 and the maximal possible frequency shift between the local oscillators, as well as the attenuation factor introduced by the filters of the transmitter and receiver), the local oscillator frequency difference Δf_{lo}^q will not affect the system synchronization, leaving only the constant delay difference $\tau_{meas}^{i,j} - \tau_{ref}$ and the constant complex amplitude $\sigma_{meas}^{i,j}$, which, however, can be easily compensated in the data preprocessing step. In other words, since the common-clocked reference and measurement signals are affected by the same frequency offset between transmitter and receiver, computing the element-wise inversion of one spectrum with the other cancels this effect as long as this frequency offset remains small with respect to the recorded bandwidth, helping the SDR-GBIR system to be synchronized.

For example, as to the SFCW signal, a single-frequency signal will be transmitted in each TR routine with the bandwidth of $B_0 = 0$. Therefore, by selecting the maximum of Eq. (10), we can get a signal element $S_u^{i,j,q}$ as

$$\begin{aligned} S_u^{i,j,q} &= S^{i,j,q}(f=\Delta f_{lo}^q) \\ &= \sigma_D^{i,j,q}e^{-j2\pi f_{lo}^{1,q}(\tau_D^{i,j}-\tau_{ref})} \\ &+ \sum_{n=1}^{N}\sigma_n^{i,j,q}e^{-j2\pi f_{lo}^{1,q}(\tau_n^{i,j}-\tau_{ref})} \end{aligned} \tag{11}$$

For the FMCW signal or the NW signal, the signal bandwidth in each TR routine can be determined by $B_0 = \gamma T$ or $B_0 = 1/\tau_c$, which satisfies $B_0 \le f_s$, where $f_s = 1/\Delta T$ is the data sampling rate. Therefore, by only selecting the frequencies that satisfy $-f_s/2 \le -B_0/2 \le -B_u/2 \le f_u \le B_u/2 \le B_0/2 \le f_s/2$, we can get a signal vector $\boldsymbol{S}_u^{i,j,q}$ whose

p-th element can be expressed as

$$\begin{aligned}S_{u,p}^{i,j,q} &= S^{i,j,q}(f_u = -B_u/2 + (p-1)\delta f) \\ &= \sigma_D^{i,j,q} e^{-j2\pi(-B_u/2+(p-1)\delta f + f_{lo}^{2,q})(\tau_D^{i,j}-\tau_{ref})} \\ &+ \sum_{n=1}^{N} \sigma_n^{i,j,q} e^{-j2\pi(-B_u/2+(p-1)\delta f + f_{lo}^{2,q})(\tau_n^{i,j}-\tau_{ref})}\end{aligned} \tag{12}$$

where $\delta f = 1/T$, $p = 1, 2, ..., P$, $P = B_u T$ denotes the number of the selected frequencies, and, without loss of generality, P is defined as an even number in the derivation of Eq. (12).

It can be seen from Eqs. (11) and (12), the signal element $S_u^{i,j,q}$ and the signal vector $\boldsymbol{S}_u^{i,j,q}$ are not related to Δf_{lo}^q and contains all the necessary information for the following process. Therefore, it can be concluded that the SDR-GBIR system can be easily synchronized with the proposed scheme. Here, it should be also noted that, different from Eq. (11) whose phase term is dependent on the known $f_{lo}^{1,q}$, the phase term in Eq. (12) is dependent on the known $f_{lo}^{2,q}$ and B_u as no maximum selection can be conducted for FMCW signal and NW signal.

B. Bandwidth synthesis

As mentioned in Section II-B, the frequency-domain bandwidth synthesis method will be used by SDR-GBIR to get a high range resolution, which is detailed here.

Firstly, considering the SFCW signal with $\Delta f_{lo}^{q+1} - \Delta f_{lo}^q = \Delta f$ and Δf as a constant frequency step, we can get a signal vector from Q TR routines (i.e., Q carrier frequencies) based on Eq. (11) as

$$\begin{aligned}\boldsymbol{S}^{i,j} &= [S_u^{i,j,1}, S_u^{i,j,2}, ..., S_u^{i,j,Q}]^T \\ &= \boldsymbol{S}_D^{i,j} + \boldsymbol{S}_T^{i,j} \in C^{Q\times 1}\end{aligned} \tag{13}$$

where $(\cdot)^T$ denotes matrix transpose, $\boldsymbol{S}_D^{i,j}$ denotes the DPI vector, and $\boldsymbol{S}_T^{i,j}$ denotes the target vector.

According to Eq. (13) and by suppressing the DPI, a high-resolution range profile of targets can be obtained by the inverse fast Fourier transform (IFFT) as

$$\begin{aligned}\boldsymbol{r}^{i,j}(\tau) = &\sum_{n=1}^{N} \sigma_n^{i,j,q} e^{-j2\pi f_c(\tau_n^{i,j,q}-\tau_{ref})} \\ &\frac{\sin[\pi B(\tau - \tau_n^{i,j,q} + \tau_{ref})]}{\sin[\pi B(\tau - \tau_n^{i,j,q} + \tau_{ref})/Q]}\end{aligned} \tag{14}$$

where $f_c = f_{lo}^{1,1} + (Q-1)\Delta f/2$ denotes the center frequency and $B = Q\Delta f$ denotes the bandwidth of the SFCW signal whose range resolution is thus given by $\delta r = c/2B$, where c denotes the speed of light. For SFCW signal, the maximal detection range is determined by $r_d = c/2\Delta f$. Hence, a smaller Δf gives a larger detection range, which, however, results in a longer measurement duration if the same bandwidth is desired.

Alternatively, according to Eq. (12), for the FMCW signal and NW signal, by setting the frequency step as $\Delta f = B_u$, we can get a signal vector from Q TR routines as

$$\begin{aligned}\boldsymbol{S}^{i,j} &= [(\boldsymbol{S}_u^{i,j,1})^T, (\boldsymbol{S}_u^{i,j,2})^T, ..., (\boldsymbol{S}_u^{i,j,Q})^T]^T \\ &= \boldsymbol{S}_D^{i,j} + \boldsymbol{S}_T^{i,j} \in C^{O\times 1}\end{aligned} \tag{15}$$

based on which a high-resolution range profile of targets can be obtained as

$$\begin{aligned}\boldsymbol{r}^{i,j}(\tau) = &\sum_{n=1}^{N} \sigma_n^{i,j,q} e^{-j2\pi f_c(\tau_n^{i,j,q}-\tau_{ref})} \\ &\frac{\sin[\pi B(\tau - \tau_n^{i,j,q} + \tau_{ref})]}{\sin[\pi B(\tau - \tau_n^{i,j,q} + \tau_{ref})/O]}\end{aligned} \tag{16}$$

where $f_c = f_{lo}^{2,1} - B_u/2 + (O-1)\delta f/2$ denotes the center frequency, $O = PQ$, and $B = O\delta f$ denotes the signal bandwidth. Therefore, with $O\delta f = Q\Delta f$, it can be derived that, although the range resolution and the measurement duration are the same, the maximal detection range of the FMCW signal and the NW signal is increased to $r_d = Pc/2\Delta f$, i.e., P times larger than the SFCW signal.

Eqs. (14) and (16) indicate that, by using the frequency-domain bandwidth synthesis method, wide bandwidth and thus high range resolution can be achieved.

C. Data preprocessing

In practice, non-ideal factors, i.e., the DPI $\boldsymbol{S}_D^{i,j}$ in $\boldsymbol{S}^{i,j}$ and the intrinsic delay/amplitude of the measurement channel, will introduce seriously negative effects on the system performance of SDR-GBIR. Therefore, data preprocessing is important to get rid of these influences before target imaging and displacement measurement.

For SDR-GB-SAR, with proper setup (e.g., using the similar connection cables for the reference and measurement channels and physically isolating the TR antennas or setting one antenna at the null radiation direction of the other), we have $\tau_{meas}^{i,j} \triangleq \tau_{meas} \approx \tau_{ref}$, $\sigma_{meas}^{i,j,q} \triangleq \sigma_{meas}^q \approx \sigma_{ref}$, and $\sigma_{D,0}^{i,j} \approx 0$. Then, the DPI component and the intrinsic delay-amplitude of the measurement channel will have relatively small impacts on the following process. However, these tricks cannot be used for highly accurate measurements. Besides, for SDR-GB-MIMO radar, the two 1×8 switches will introduce different delays and amplitudes for different measurement channels, and closely-located TR antennas will introduce significant DPIs even in the condition of normal physical isolation. Therefore, some processing methods are needed to suppress the DPI and to compensate the delay-amplitude difference among different channels. In the following, we use the SFCW signal as an example to explain how can we achieve the DPI suppressed and delay-amplitude compensated signal.

Firstly, by connecting the transmitting and receiving channels through an attenuator directly, we can get the following calibration signal as

$$s_c^{i,j,q}(t) = \sigma_c^{i,j,q} s_0(t - \tau_c^{i,j}) e^{j2\pi[\Delta f_{lo}^q t - f_{lo}^{1,q}\tau_c^{i,j}] + j\psi_0^{i,j,q}} \tag{17}$$

where $\sigma_c^{i,j,q} \approx F\sigma_{meas}^{i,j,q}$ with F as the constant attenuation coefficient and $\tau_c^{i,j} \approx \tau_{meas}^{i,j}$.

Then, by transforming the calibration signal to the frequency domain, we get

$$S_c^{i,j,q}(f) = S_0(f - \Delta f_{lo}^q)e^{j\psi_0^{i,j,q}}\sigma_c^{i,j,q}e^{-j2\pi(f+f_{lo}^{2,q})\tau_c^{i,j}} \quad (18)$$

Based on Eq. (18), we can get the signal vector $\boldsymbol{S}_c^{i,j} \in C^{Q\times 1}$ according to Eq. (13), whose q-th element can be expressed as

$$\begin{aligned} \boldsymbol{S}_C^{i,j}(q) &= S_c^{i,j,q}(\Delta f_{lo}^q)/S_r^{i,j,q}(\Delta f_{lo}^q) \\ &= \sigma_c^{i,j,q}e^{-j2\pi f_{lo}^{1,q}(\tau_c^{i,j}-\tau_{ref})} \end{aligned} \quad (19)$$

Therefore, the following relationships can be satisfied

$$\begin{cases} \boldsymbol{S}_D^{i,j}(q)/\boldsymbol{S}_C^{i,j}(q) = \sigma_{D,0}^{i,j}/Fe^{-j2\pi f_{lo}^{1,q}\tau_{D,0}^{i,j}} \\ \boldsymbol{S}_T^{i,j}(q)/\boldsymbol{S}_C^{i,j}(q) = \frac{1}{F}\sum\limits_{n=1}^{N}\sigma_n^0 e^{-j2\pi f_{lo}^{1,q}\tau_{n,0}^{i,j}} \end{cases} \quad (20)$$

According to Eq. (20) and considering it is much more significant than other components, the DPI in $\boldsymbol{S}^{i,j}$ can be suppressed by the LS based method [25], [26] as

$$\widetilde{\boldsymbol{S}}^{i,j} = \boldsymbol{S}^{i,j} - \boldsymbol{G}(\boldsymbol{G}^H\boldsymbol{G})^{-1}\boldsymbol{G}^H\boldsymbol{S}^{i,j} \quad (21)$$

where $(\cdot)^H$ denotes matrix conjugate transpose, $(\cdot)^{-1}$ denotes matrix inverse, and $\boldsymbol{G} \in C^{Q\times L}$ is constructed by the delayed copies of $\boldsymbol{S}_C^{i,j}$ in the frequency domain, given by

$$\boldsymbol{G} = [(\boldsymbol{S}_C^{i,j} \odot e^{-j2\pi\boldsymbol{f}\tau_1}), ..., (\boldsymbol{S}_C^{i,j} \odot e^{-j2\pi\boldsymbol{f}\tau_L})] \quad (22)$$

with $\odot$ as the Hadamard product, $\boldsymbol{f} = [f_{lo}^{1,1}, f_{lo}^{1,2}, ..., f_{lo}^{1,Q}]^T$, and $[\tau_1, ..., \tau_L]$ as the discrete time delay list used to properly model the DPI.

At last, given $\widetilde{\boldsymbol{S}}^{i,j}$, the delay-amplitude difference can be compensated by

$$\widehat{\boldsymbol{S}}^{i,j} = \widetilde{\boldsymbol{S}}^{i,j}/\boldsymbol{S}_C^{i,j} \approx \frac{1}{F}\sum_{n=1}^{N}\sigma_n^0 e^{-j2\pi\boldsymbol{f}\tau_{n,0}^{i,j}} \quad (23)$$

Actually, an alternative approach based on atomic norm minimization and Vandermonde decomposition [25] can be used for DPI suppression after delay-amplitude compensation. In such a case, we first get the DPI-included but delay-amplitude compensated signal vector as

$$\boldsymbol{S}_0^{i,j} = \boldsymbol{S}^{i,j}/\boldsymbol{S}_C^{i,j} = \boldsymbol{S}_{D,0}^{i,j} + \boldsymbol{S}_{T,0}^{i,j} \quad (24)$$

where $\boldsymbol{S}_{D,0}^{i,j} = \sigma_{D,0}^{i,j}/Fe^{-j2\pi\boldsymbol{f}\tau_{D,0}^{i,j}}$. Then, by formulating Eq. (24) as a 1D frequency estimation problem, the DPI component in $\boldsymbol{S}_0^{i,j}$ can be estimated by solving

$$\begin{aligned} &[\widetilde{\boldsymbol{S}}_{D,0}^{i,j}, \widetilde{\boldsymbol{u}}] = \min_{\boldsymbol{S}_D^{i,j}, \boldsymbol{u}} \mathrm{trace}[T(\boldsymbol{u})] \\ &s.t. \begin{bmatrix} 1 & (\boldsymbol{S}_{D,0}^{i,j})^H \\ \boldsymbol{S}_{D,0}^{i,j} & T(\boldsymbol{u}) \end{bmatrix} \geq 0, ||\boldsymbol{S}_0^{i,j} - \boldsymbol{S}_{D,0}^{i,j}||_2^2 \leq \varepsilon_n \end{aligned} \quad (25)$$

where trace$[\,\cdot\,]$ denotes the trace of a matrix, $T(\boldsymbol{u})$ denotes a Toeplitz matrix formed by the vector $\boldsymbol{u}$, and ε_n denotes the target plus noise power level.

After solving Eq. (25) and conducting Vandermonde decomposition and LS based amplitude estimation to get the DPI approximation $\widetilde{\boldsymbol{S}}_{D,0}^{i,j}$, the DPI component in $\boldsymbol{S}_0^{i,j}$ can be suppressed, giving us

$$\widehat{\boldsymbol{S}}^{i,j} = \boldsymbol{S}_0^{i,j} - \widetilde{\boldsymbol{S}}_{D,0}^{i,j} \approx \frac{1}{F}\sum_{n=1}^{N}\sigma_n^0 e^{-j2\pi\boldsymbol{f}\tau_{n,0}^{i,j}} \quad (26)$$

We note that, in comparison with the method in Eq. (23), the method in Eq. (26) is more effective on suppressing the DPI but also more time-consuming. Therefore, we used the former method in the experiments, which works well as observed. Besides, the reasons why DPI suppression is not conducted in the time domain are: 1) the intrinsic amplitude of the measurement channel is assumed to be frequency-dependent, hence it is better to be processed in the frequency domain, and 2) the delay of DPI is not exactly integral times of the data sampling interval ΔT, making the methods working in the time domain cannot mitigate the DPI component effectively (consider that a 2-MS/s sampling rate gives a sampling interval of 150 m, which is much larger than the DPI delay). Furthermore, although the above derivations are conducted based on the SFCW signal, there is no problem when applied to the FMCW and NW signals, as all these three signals have the same model in the frequency domain.

D. High-resolution imaging

After data preprocessing, high-resolution imaging should be performed to get the focused image of the observation scene to distinguish different targets. For GBIR target imaging, back projection algorithm (BPA), range migration algorithm (RMA), and far-field pseudo-polar format algorithm (FPFA) are commonly used [34]–[36]. Compared with other algorithms, BPA is more universal as it can be used without geometric limitations and approximations, hence is selected for SDR-GBIR in this study to not limit its system flexibility. In the following, again, we use the SFCW signal as an example to explain how to obtain a high-quality target image, which can also be applied to the cases with FMCW and NW signals.

Firstly, according to Eq. (23), the signal vector echoed from all the targets in the observation scene measured at all frequencies and antenna positions can be written as

$$\boldsymbol{y} = [(\widehat{\boldsymbol{S}}^{1,1})^T, (\widehat{\boldsymbol{S}}^{1,2})^T, ..., (\widehat{\boldsymbol{S}}^{I,J})^T]^T \in C^{IJQ\times 1} \quad (27)$$

whose $[(i-1)JQ + (j-1)Q + q]$-th element can be expressed as

$$\begin{aligned} \boldsymbol{y}^{i,j,q} &= \iiint_{\Omega} \sigma_{x,y,z}e^{-j2\pi f_q\tau_{x,y,z}^{i,j}}dxdydz + n_{i,j,q} \\ &\approx \sum_{u=1}^{U}\sum_{v=1}^{V}\sum_{w=1}^{W}\sigma_{x_u,y_v,z_w}e^{-j2\pi f_q\tau_{x_u,y_v,z_w}^{i,j}} + n_{i,j,q} \end{aligned} \quad (28)$$

where Ω denotes the observation scene, $f_q \triangleq f_{lo}^{1,q}$, $n_{i,j,q}$ denotes the noise, U, V, and W denote the numbers of the discretization grids in the x, y, and z directions, σ_{x_u,y_v,z_w} denotes the amplitude of the target at (x_u, y_v, z_w) with a gain of $1/F$, and $\tau^{i,j}_{x_u,y_v,z_w}$ denotes its delay with respect to the i-th transmitting antenna at (x_i, y_i, z_i) and j-th receiving antenna at (x_j, y_j, z_j), given by

$$\tau^{i,j}_{x_u,y_v,z_w} = [R^i_{x_u,y_v,z_w} + R^j_{x_u,y_v,z_w}]/c \tag{29}$$

with $R^i_{x_u,y_v,z_w} = [(x_i - x_u)^2 + (y_i - y_v)^2 + (z_i - z_w)^2]^{1/2}$ and $R^j_{x_u,y_v,z_w} = [(x_j - x_u)^2 + (y_j - y_v)^2 + (z_j - z_w)^2]^{1/2}$.

Then, the signal vector $\boldsymbol{y}$ can be rewritten as

$$\boldsymbol{y} = \boldsymbol{\Phi}\boldsymbol{\sigma} + \boldsymbol{n} \tag{30}$$

with $\boldsymbol{\sigma} = [\sigma_{x_1,y_1,z_1}, \sigma_{x_1,y_1,z_2}, ..., \sigma_{x_U,y_V,z_W}] \in C^{UVW\times 1}$, $\boldsymbol{n} = [n_{1,1,1}, n_{1,1,2}, ..., n_{I,J,Q}] \in C^{IJQ\times 1}$, and

$$\boldsymbol{\Phi} = \begin{bmatrix} e^{-j2\pi \boldsymbol{f} \tau^{1,1}_{x_1,y_1,z_1}} & \cdots & e^{-j2\pi \boldsymbol{f} \tau^{1,1}_{x_U,y_V,z_W}} \\ \vdots & \ddots & \vdots \\ e^{-j2\pi \boldsymbol{f} \tau^{I,J}_{x_1,y_1,z_1}} & \cdots & e^{-j2\pi \boldsymbol{f} \tau^{I,J}_{x_U,y_V,z_W}} \end{bmatrix} \tag{31}$$

By coherently summing the signals at all antenna positions and frequencies, the amplitude of the target at (x_u, y_v, z_w) can be estimated by BPA as

$$\boldsymbol{\sigma}^{BP}_{x_u,y_v,z_w} = \frac{1}{IJQ}\sum_{i=1}^{I}\sum_{j=1}^{J}\sum_{q=1}^{Q} \boldsymbol{y}^{i,j,q} e^{+j2\pi f_q \tau^{i,j}_{x_u,y_v,z_w}} \tag{32}$$

Therefore, the vectorized amplitudes of all targets can be estimated by

$$\boldsymbol{\sigma}^{BP} = \frac{1}{IJQ}\boldsymbol{\Phi}^H \boldsymbol{y} \tag{33}$$

It can be seen from Eq. (33) that the BPA uses $\frac{1}{IJQ}\boldsymbol{\Phi}^H$ to approximate the inverse of $\boldsymbol{\Phi}$ to solve Eq. (30). If the columns of $\boldsymbol{\Phi}$ are orthogonal (or near orthogonal) to each other, i.e., $\frac{1}{IJQ}\boldsymbol{\Phi}^H\boldsymbol{\Phi} \approx \boldsymbol{I}$, where $\boldsymbol{I}$ is the unit matrix, and the targets are located exactly at the discretized grids, Eq. (33) can get a well-focused target image. If the grid size is decreased to more accurately locate the targets, i.e., UVW becomes (much) bigger than IJQ, the columns of $\boldsymbol{\Phi}$ are no longer orthogonal but correlated, resulting in high-level sidelobes in the obtained target image. Sidelobes of strong targets may make the weak targets undetectable and sidelobes of multiple targets produce spurious peaks, resulting in negative effects on the following processing, i.e., displacement estimation in our case. To improve the imaging resolution and avoid sidelobes, a popular approach is to explore the sparsity of $\boldsymbol{\sigma}$ based on the CS theory [3], [37] by solving the following minimization problem

$$\boldsymbol{\sigma}^{CS} = \min ||\boldsymbol{\sigma}||_0 \quad s.t.\ ||\boldsymbol{y} - \boldsymbol{\Phi}\boldsymbol{\sigma}||_2 \le \varepsilon \tag{34}$$

where ε denotes the noise power level.

Normally, to handle the NP-hard task of solving Eq. (34), an appealing approach is to relax the L_0 norm to the L_1 norm, giving the Lasso optimization problem

$$\boldsymbol{\sigma}^{CS} = \min_{\boldsymbol{\sigma}} \frac{1}{2}||\boldsymbol{y} - \boldsymbol{\Phi}\boldsymbol{\sigma}||_2^2 + \lambda||\boldsymbol{\sigma}||_1 \tag{35}$$

where λ is the regularization parameter.

An effective way to solve Eq. (35) is to use the iterative soft thresholding algorithm (ISTA) [38], where the solution at the $[k+1]$-th iteration is given by

$$\boldsymbol{\sigma}_{k+1} = \eta_{\theta_{k+1}}[\boldsymbol{\sigma}_k + \mu_{k+1}\boldsymbol{\Phi}^H(\boldsymbol{y} - \boldsymbol{\Phi}\boldsymbol{\sigma}_k)] \tag{36}$$

with $\eta_{\theta_{k+1}}[x] = x/|x| \max(|x| - \theta_{k+1}, 0)$ as the soft shrinkage function and μ_{k+1} as the step size.

To accelerate the convergence, the fast ISTA (FISTA) is proposed in [39], whose $[k+1]$-th iteration is in the form of

$$\begin{cases} \boldsymbol{\sigma}_{k+1} = \eta_{\theta_{k+1}}[\boldsymbol{\rho}_k + \mu_{k+1}\boldsymbol{\Phi}^H(\boldsymbol{y} - \boldsymbol{\Phi}\boldsymbol{\rho}_k)] \\ \xi_{k+1} = (1 + \sqrt{1 + 4\xi_k^2})/2 \\ \boldsymbol{\rho}_{k+1} = \boldsymbol{\sigma}^{k+1} + \frac{\xi_k - 1}{\xi_{k+1}}(\boldsymbol{\sigma}_{k+1} - \boldsymbol{\sigma}_k) \end{cases} \tag{37}$$

However, with large values of IJQ and UVW, the computational cost and memory usage of Eq. (37) are normally beyond the computing capacity of a general personal computer, making it unsuitable for SDR-GBIR target imaging in practice. Therefore, inspired by the approximated CS based methods [40], [41] and based on FISTA, we propose a method to solve Eq. (35) effectively, giving an imaging method for SDR-GBIR to get high-resolution target images with low computational cost and small memory usage.

In general, considering that the most time-consuming parts in Eq. (37) are the two matrix-vector multiplications $\boldsymbol{\Phi}^H\boldsymbol{b}_k$ and $\boldsymbol{a}_k = \boldsymbol{\Phi}\boldsymbol{\rho}_k$, where $\boldsymbol{b}_k = \boldsymbol{y} - \boldsymbol{a}_k$, we try to more effectively calculate $\boldsymbol{c}_k = \boldsymbol{\Phi}^H\boldsymbol{b}_k$ and $\boldsymbol{a}_k$ without loading $\boldsymbol{\Phi}$ in each iteration to also save the memory usage. At first, it can be easily deirved that the $[(u-1)VW + (v-1)W + w]$-th element of $\boldsymbol{c}_k$ is actually obtained by

$$\boldsymbol{c}_k^{u,v,w} = \sum_{i=1}^{I}\sum_{j=1}^{J}\sum_{q=1}^{Q} \boldsymbol{b}_k^{i,j,q} e^{+j2\pi f_q \tau^{i,j}_{x_u,y_v,z_w}} \tag{38}$$

where $\boldsymbol{b}_k^{i,j,q}$ denotes the $[(i-1)JQ + (j-1)Q + q]$-th element of $\boldsymbol{b}_k$, similar to the BPA shown in Eq. (32).

Hence, Eq. (38) can be accelerated by using IFFT and sinc interpolation, which is normally applied by the BPA working in the time domain [3], giving

$$\boldsymbol{c}_k^{u,v,w} = \sum_{i=1}^{I}\sum_{j=1}^{J} \mathcal{I}_{\text{sinc}}[\mathcal{F}_{\text{inv}}(\boldsymbol{b}_k^{i,j}, M) \odot \boldsymbol{\alpha}, \tau^{i,j}_{x_u,y_v,z_w}]\boldsymbol{\beta}^{i,j}_{x_u,y_v,z_w} \tag{39}$$

where $\mathcal{F}_{\text{inv}}(\cdot, M)$ denotes IFFT with the length of M (typically a power of 2), $\boldsymbol{\alpha} \in C^{M\times 1}$ with its m-th element as $\boldsymbol{\alpha}_m = e^{-j\pi(m-1)(Q-1)/M}$, $\boldsymbol{\beta}^{i,j}_{u,v,w} = e^{j2\pi f_c \tau^{i,j}_{x_u,y_v,z_w}}$, and

$\mathcal{I}_{\text{sinc}}[\cdot, \tau^{i,j}_{x_u,y_v,z_w}]$ denotes the sinc interpolation at $\tau^{i,j}_{x_u,y_v,z_w}$. Therefore, $\boldsymbol{c}_k$ can be obtained by

$$\boldsymbol{c}_k = \sum_{i=1}^{I}\sum_{j=1}^{J}\mathcal{I}_{\text{sinc}}[\mathcal{F}_{\text{inv}}(\boldsymbol{b}_k^{i,j}, M)\odot\boldsymbol{\alpha}, \boldsymbol{\tau}^{i,j}]\odot\boldsymbol{\beta}^{i,j} \tag{40}$$

with $\boldsymbol{\tau}^{i,j} = [\tau^{i,j}_{x_1,y_1,z_1}, \tau^{i,j}_{x_1,y_1,z_2}, ..., \tau^{i,j}_{x_U,y_V,z_W}] \in C^{UVW\times 1}$ and $\boldsymbol{\beta}^{i,j} = [\beta^{i,j}_{1,1,1}, \beta^{i,j}_{1,1,2}, ..., \beta^{i,j}_{U,V,W}] = e^{j2\pi f_c\boldsymbol{\tau}^{i,j}}$.

To be more time-saving, the Type-II non-uniform FFT (NUFFT) with fast Gaussian gridding [42], [43] working with uniform frequencies but non-uniform delays can be employed to replace the IFFT and sinc interpolation, giving

$$\boldsymbol{c}_k = \sum_{i=1}^{I}\sum_{j=1}^{J}\mathcal{N}_{\text{II}}[\boldsymbol{b}_k^{i,j}, 2\pi\Delta f\boldsymbol{\tau}^{i,j}]\odot\boldsymbol{\beta}^{i,j} \tag{41}$$

where $\mathcal{N}_{\text{II}}[FK, XJ]$ denotes the Type-II NUFFT with FK as the input Fourier coefficient values and XJ as the location of output values.

Similarly, it can be derived that the $[(i-1)JQ+(j-1)Q+q]$-th element of $\boldsymbol{a}_k$ is actually obtained by

$$\boldsymbol{a}_k^{i,j,q} = \sum_{u=1}^{U}\sum_{v=1}^{V}\sum_{w=1}^{W}\boldsymbol{\rho}_k^{u,v,w}e^{-j2\pi f_q\tau^{i,j}_{x_u,y_v,z_w}} \tag{42}$$

Therefore, the signal vector $\boldsymbol{a}_k^{i,j} \in C^{Q\times 1}$ with respect to the i-th transmitting antenna and j-th receiving antenna can be obtained by the Type-I NUFFT working with non-uniform delays but uniform frequencies, giving

$$\boldsymbol{a}_k^{i,j} = UVW\mathcal{N}_{\text{I}}[\boldsymbol{\rho}_k\odot(\boldsymbol{\beta}^{i,j})^*, 2\pi\Delta f\boldsymbol{\tau}^{i,j}, Q] \tag{43}$$

where $\mathcal{N}_{\text{I}}[CJ, XJ, MS]$ denotes the Type-I NUFFT with CJ as the strengths of sources, XJ as the location of sources, and MS as the number of output values [42], [43].

Based on Eqs. (41) and (43), we can solve the Lasso optimization problem in Eq. (35) effectively with the FISTA for SDR-GBIR high-resolution and high-quality target imaging. Since it is based on NUFFT and FISTA, we call the proposed imaging method as NUFFT-FISTA, whose detailed implementation is summarized in Table. I.

Compared to the calculations shown in Eq. (37), since the matrix-vector multiplications are replaced with NUFFTs in the proposed method, there is no need to construct $\boldsymbol{\Phi}$, only $\boldsymbol{\tau}^{i,j}$ with $i = 1, 2, ..., I$ and $j = 1, 2, ..., J$ needs to be saved and loaded, hence significantly reducing the storage cost (from $IJQ\times UVW$ to $IJ\times UVW$). Besides, in each iteration of FISTA, the computational complexity in terms of multiplications is changed from $2IJQUVW$ to $2IJ[(4M_{sp}+1)UVW + Q_r log_2(Q_r)]$ with M_{sp} as the spreading parameter and $Q_r = CQ$, where C is the oversampling ratio [42], [44]. When Q is large, which is normally the case in order to obtain a high range resolution, the computational cost can also be much reduced by the proposed method. In summary, although the proposed imaging method is only a simple modification of FISTA, it is more suitable for GBIR target imaging in practice.

TABLE I
NUFFT-FISTA FOR SDR-GBIR TARGET IMAGING.

```
Input: y, θ, μ, max iteration number K, and stop parameter ς
Initial: σ_0 = 0, ρ_0 = 0, and ξ_0 = 1
for k = 0 to K − 1 do
  for i = 1 to I do
    for j = 1 to J do
      a_k^{i,j} = UVW N_I[ρ_k ⊙ (β^{i,j})^*, 2πΔf τ^{i,j}, Q]
    end for
  end for
  b_k = y − a_k
  c_k = Σ_{i=1}^{I} Σ_{j=1}^{J} N_II[b_k^{i,j}, 2πΔf τ^{i,j}] ⊙ β^{i,j}
  σ_{k+1} = η_{θ_{k+1}}[ρ_k + μ_{k+1} c_k]
  ξ_{k+1} = (1 + sqrt(1 + 4ξ_k^2))/2
  ρ_{k+1} = σ^{k+1} + (ξ_k − 1)/ξ_{k+1} (σ_{k+1} − σ_k)
  if |σ^{k+1} − σ^k|_2/|σ^k|_2 < ς then
    K_0 = k + 1
    stop iteration
  end if
end for
Return: σ_{K_0} or σ_K
```

Beyond high-resolution and low sidelobe level, another advantage of the proposed imaging method lies on the reduction of measurement duration for SDR-GBIR. Based on the CS theory, $\boldsymbol{\sigma}$ can be estimated from Eq. (35) with under-sampled data. Thanks to this, we can reduce the number of frequencies (Q) for bandwidth synthesis and reduce the numbers of antenna positions (I and J) without affecting the performance of SDR-GBIR, hence reduce the measurement duration. In such a case, by randomly selecting $Q_1 \leq Q$ carrier frequencies in a given bandwidth B and selecting $I_1 \leq I$ and $J_1 \leq J$ antenna positions in a given aperture or given TR arrays, we get the optimization problem for SDR-GBIR target imaging as

$$\boldsymbol{\sigma}^{CS} = \min_{\boldsymbol{\sigma}}\frac{1}{2}||\boldsymbol{y}_1 - \boldsymbol{\Phi}_1\boldsymbol{\sigma}||_2^2 + \lambda||\boldsymbol{\sigma}||_1 \tag{44}$$

where $\boldsymbol{y}_1 \in C^{I_1J_1Q_1\times 1}$ is the under-sampled data after preprocessing (note that the methods for DPI suppression and delay-amplitude compensation shown in Eq. (23) and Eq. (26) can still work well with under-sampled frequencies [25]) and $\boldsymbol{\Phi}_1 \in C^{I_1J_1Q_1\times UVW}$ is obtained by only selecting the rows of $\boldsymbol{\Phi}$ corresponding to the sampled frequencies and antenna positions with $I_1J_1Q_1 \ll IJQ$.

To solve Eq. (44), a natural approach is to use the same processing flow given in Table. I by making $\boldsymbol{b}_k^{(i,j,q)\in\Gamma} = \boldsymbol{y}_1 - \boldsymbol{a}_k^{(i,j,q)\in\Gamma}$ and $\boldsymbol{b}_k^{(i,j,q)\notin\Gamma} = 0$, where $\Gamma \in R^{I_1J_1Q_1\times 1}$ is the indexes of selected frequencies and antenna positions [45]. An alternative approach is to use the Type-III NUFFT working with non-uniform inputs and non-uniform outputs to calculate $\boldsymbol{a}_k$ and $\boldsymbol{c}_k$ directly, i.e.,

$$\begin{cases} \boldsymbol{a}_k^{i_1,j_1} = \mathcal{N}_{\text{III}}[\boldsymbol{\rho}_k\odot(\boldsymbol{\beta}_1^{i_1,j_1})^*, 2\pi\boldsymbol{\tau}_1^{i_1,j_1}\Delta f, \frac{\boldsymbol{f}_1 - f_c}{\Delta f}] \\ \boldsymbol{b}_k = \boldsymbol{y}_1 - \boldsymbol{a}_k \\ \boldsymbol{c}_k = \sum_{i_1=1}^{I_1}\sum_{j_1=1}^{J_1}\mathcal{N}_{\text{III}}[\boldsymbol{b}_k^{i_1,j_1}, \frac{2\pi(\boldsymbol{f}_1 - f_c)}{Q\Delta f}, \boldsymbol{\tau}_1^{i_1,j_1}Q\Delta f]\odot\boldsymbol{\beta}_1^{i_1,j_1} \end{cases} \tag{45}$$

where $\mathcal{N}_{\text{III}}[CJ, XJ, SK]$ denotes the Type-III NUFFT with CJ as the strengths of sources, XJ as the location of sources, and SK as the locations of output values, $\boldsymbol{f}_1$ denotes the vector of selected frequencies, $\boldsymbol{\tau}_1$ is obtained from $\boldsymbol{\tau}$ corresponding to the selected antennas, and $\boldsymbol{\beta}_1^{i_1,j_1} = e^{j2\pi f_c \boldsymbol{\tau}_1^{i_1,j_1}}$.

E. Interferometric process

Based on the BPA or the proposed imaging method, a 2D or 3D complex image of the observation scene can be obtained by turning the vectorized complex amplitudes $\boldsymbol{\sigma}$ to a matrix or a tensor. The amplitude of the image can be used to interpret the scattering properties of the observed scene (i.e., to differentiate targets with potential displacements) while the phase of the image can be exploited to measure the target displacement when a temporal baseline is introduced.

Assuming $\boldsymbol{I}_M$ and $\boldsymbol{I}_S$ are the two images obtained at different time, their phase difference can be calculated to generate an interferogram as $\Delta\boldsymbol{\Psi} = \arg[\boldsymbol{I}_S(\boldsymbol{I}_M)^*]$, where $\arg[\cdot]$ denotes the argument of a complex value. Then, to evaluate the quality of the interferogram, a coherence image can be generated [46], whose $[u,v,w]$-th element is given by

$$\Upsilon^{u,v,w} = \frac{\left|E\left\{I_S^{u,v,w}(I_M^{u,v,w})^*\right\}\right|}{\sqrt{E\left\{|I_S^{u,v,w}|^2\right\}E\left\{|I_M^{u,v,w}|^2\right\}}} \tag{46}$$

where $E\{\cdot\}$ denotes the expectation.

In practice, the expectation operation in Eq. (46) is always approximated by a moving average process, i.e.,

$$\widetilde{\Upsilon}^{u,v,w} = \frac{\left|\sum\limits_{l_1}\sum\limits_{l_2}\sum\limits_{l_3} g_S^{l_1,l_2,l_3}\left(g_M^{l_1,l_2,l_3}\right)^*\right|}{\sqrt{\sum\limits_{l_1}\sum\limits_{l_2}\sum\limits_{l_3}\left|g_S^{l_1,l_2,l_3}\right|^2\left|g_M^{l_1,l_2,l_3}\right|^2}} \tag{47}$$

where $g_S^{l_1,l_2,l_3} = I_S^{u+l_1,v+l_2,w+l_3}$, $g_M^{l_1,l_2,l_3} = I_M^{u+l_1,v+l_2,w+l_3}$, $l_1 \in [-L_1/2, L_1/2]$, $l_2 \in [-L_2/2, L_2/2]$, and $l_3 \in [-L_3/2, L_3/2]$ with $L_1 \times L_2 \times L_3$ as the size of the moving window.

Since GBIR can only get an accurate displacement estimation for the target with a high coherence value (i.e., with a low phase noise), target selection is conducted by thresholding the interferogram based on the coherence image, resulting in

$$\Delta\boldsymbol{\Psi}_T = \Delta\boldsymbol{\Psi}_{\boldsymbol{\Upsilon}\geq\Upsilon_T} \tag{48}$$

where Υ_T is a user-defined threshold to balance the interferogram quality and the spatial density of the selected targets.

At last, after phase unwrapping and atmospheric phase compensation (see [1] and the references therein), which give us $\Delta\widetilde{\boldsymbol{\Psi}}_T$, the target displacements along the radar line of sight (LOS) direction can be estimated by

$$\boldsymbol{d}_T = c\Delta\widetilde{\boldsymbol{\Psi}}_T \big/ 4\pi f_c \tag{49}$$

V. Experiment results

In this Section, we give some experiment results and their interpretation/analysis to show the practical performance of the developed SDR-GBIR systems and to validate the proposed preprocessing and processing methods. The experiment setups of the developed SDR-GB-SAR system and SDR-GB-MIMO radar system are shown in Fig. 5. In general, this Section mainly includes six parts: 1) demonstration of system synchronization; 2) validation of bandwidth synthesis; 3) functions of data preprocessing; 4) target 2D & 3D imaging results; 5) displacement estimation and analysis; and 6) system implementation with Wi-Fi signal.

A. Demonstration of system synchronization

At first, by assessing the phase and delay estimations of the SFCW signal, we demonstrate the synchronization of the transmitter and receiver obtained by the proposed scheme. The experiment has been conducted by directly connecting different transceiver pairs of the SDR-GB-MIMO radar system with changing carrier frequencies from 4.85 GHz to 5.15 GHz. As shown in Eq. (11) with $N = 1$, by selecting the maximum of Eq. (10), we get a complex value whose phase term is dependent on the carrier frequency $f_{lo}^{1,q}$ and the delay difference $\tau_1^{i,j} - \tau_{ref}$ (here, the DPI component is small enough to be ignored). Therefore, the phase terms corresponding to different carrier frequencies should be linearly ascending or descending if the delay difference is a constant for each specific transceiver pair. Besides, the constant delay difference should be able to be accurately estimated by the inverse Fourier transform. If the system has not been well synchronized, for each transceiver pair, the linear phase and constant delay difference assumptions are infeasible. The results shown in Fig. 6 well fit to these analysis, demonstrating the system synchronization.

B. Validation of bandwidth synthesis

Range resolution improvement obtained by bandwidth synthesis is validated by assessing the SDR-GB-SAR system using the NW signal. The spectra of the pseudo-random noise based bi-phase-coded signals with four different carrier frequencies are shown in Fig. 7, where the vertical black lines correspond to the carrier frequencies with a step of $\Delta f = 1$ MHz. Then, by selecting the frequencies satisfying $-B_u/2 \leq f_u \leq B_u/2$ with $B_u = 1$ MHz from each spectrum, a signal vector can be obtained by Eq (15), giving the range compression results shown in Fig. 8 with $Q = 1, 10, 50$ and 100. It can be seen that, via the bandwidth synthesis approach, the range resolution can be gradually improved along with the increasing number of carrier frequencies, making the reflections of different targets in the scene (tree, car, house, and so on, as shown in the left-top sub-figure of Fig. 5) more and more distinguishable in the range direction.

C. Functions of data preprocessing

With and without DPI suppression and delay-amplitude compensation, the functions of the proposed data preprocessing method are shown by assessing the SDR-GB-MIMO radar

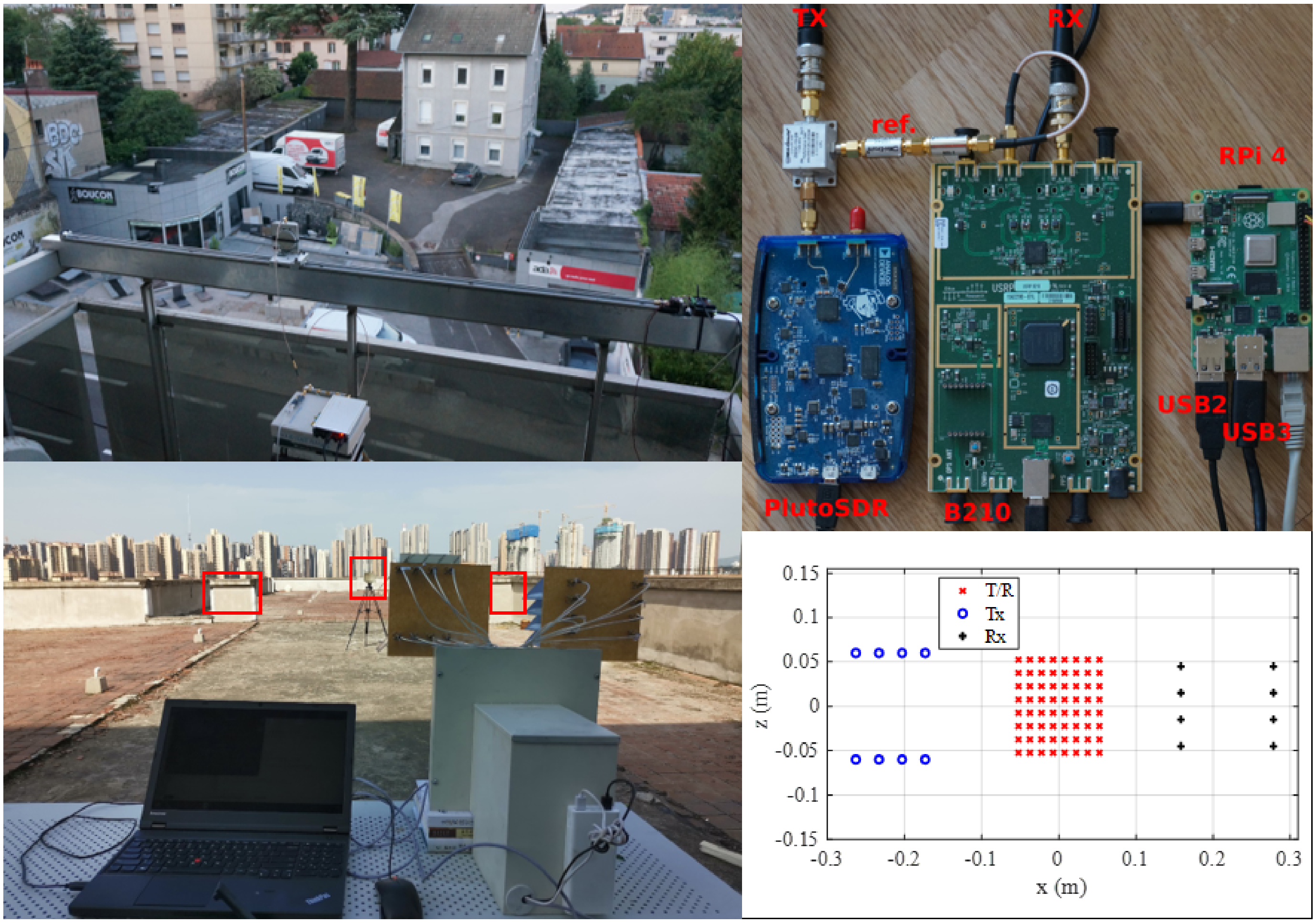

Fig. 5. Experiment setups: the left-top sub-figure corresponds to the SDR-GB-SAR system, the left-bottom sub-figure corresponds to the SDR-GB-MIMO radar system, the right-top sub-figure shows the TR subsystem of both systems, and the right-bottom sub-figure shows the antenna geometry of the SDR-GB-MIMO radar system.

system with a trihedral corner reflector (CR) and multiple walls as the targets, as indicated by the red rectangles in the left-bottom sub-figure of Fig. 5. With transmitter-1/receiver-1 (T1-R1) and transmitter-1/receiver-2 (T1-R2), the range compression results are shown in Fig. 9 and Fig. 10, respectively. It can be seen that, without applying DPI suppression based on Eq. (21), the DPI component in the measurement channel significantly affects the target detection, especially in the top sub-figure of Fig. 10. Besides, without compensating the delay-amplitude differences based on Eq. (23), the targets shifted from its true positions, as indicated by the vertical dashed line in the top sub-figure of Fig. 9. After conducting data preprocessing, the influences of DPI and delay-amplitude differences can be much reduced.

D. Target 2D & 3D imaging results

In this sub-Section, before showing the experiment results of target imaging, some simulation results are presented to validate the performance of the proposed imaging method – NUFFT-FISTA. In the simulations, the SFCW based GB-SAR signal model is used with the starting frequency of 2.4 GHz, frequency step of 0.125 MHz, frequency number of 800, antenna position number of 51, and antenna moving step of 3.06 cm (a quarter of the wavelength). In the imaging scene, 81 targets with the equivalent amplitude are uniformly distributed along the range and azimuth directions, as shown in Fig. 11. Given the SNR as 10 dB, the imaging results obtained by BPA and NUFFT-FISTA are shown in Fig. 12. It can be seen that NUFFT-FISTA can obtain a higher-quality target image that is close to the ground-truth image.

Furthermore, to confirm the advantage of NUFFT-FISTA, its comparison with BPA, orthogonal matching pursuit (OMP) algorithm [47], original FISTA, 2D OMP algorithm [48], and 2D FISTA [49] are conducted. Here, we note that, similar to FISTA, OMP is a popular algorithm used to solve the sparse vector recovery problem, while 2D FISTA and 2D OMP are their extended versions used to directly solve the sparse matrix recovery problem with reduced computational complexity and memory usage, which are suitable for GBIR imaging if some conditions can be satisfied and thus some model approximations can be used, as those in [34].

The imaging performance and the running time of different methods are evaluated with the number of randomly selected frequencies varying from 100 to 800 with a step of 50. For each frequency number and each method, 50 times simulations

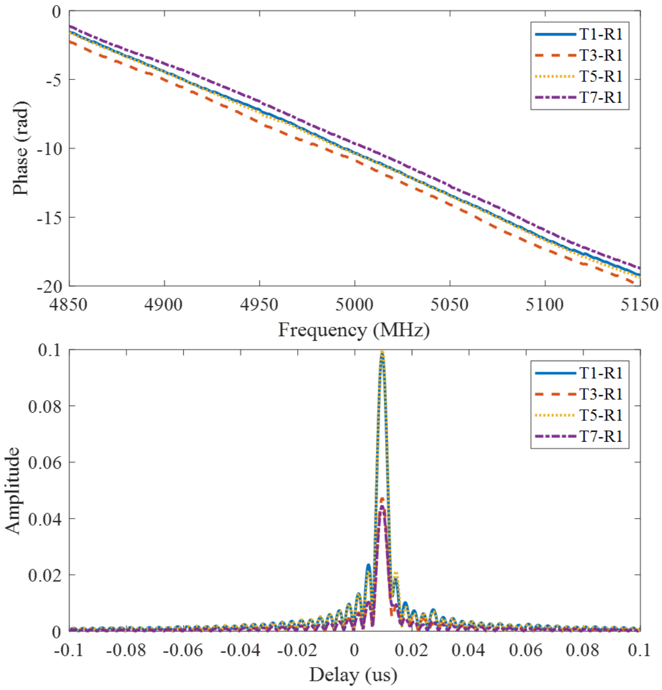

Fig. 6. System synchronization demonstrated by assessing the phase (top) and delay (bottom) estimations for different transceiver pairs of the developed SDR-GB-MIMO radar system.

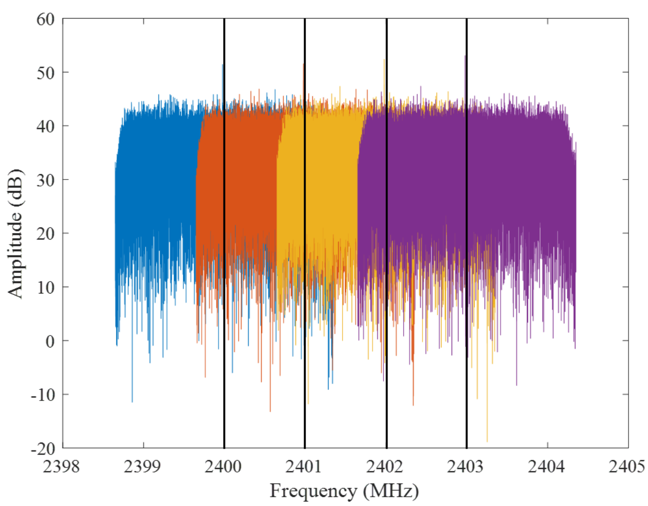

Fig. 7. Spectra of the pseudo-random noise based bi-phase-coded signals with carrier frequencies of 2400, 2401, 2402, and 2403 MHz.

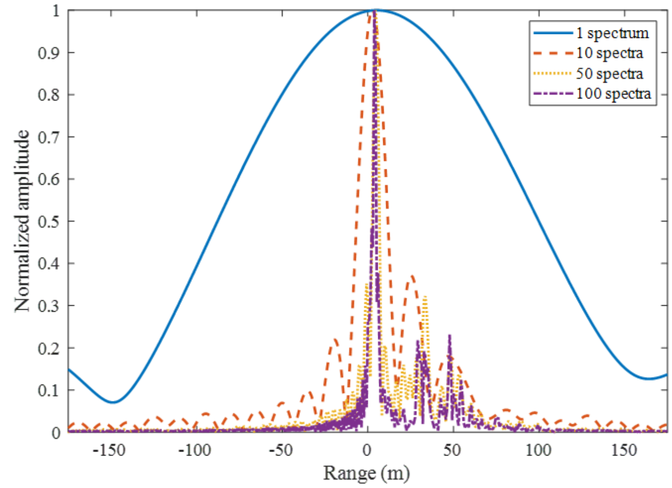

Fig. 8. Range compression results of the developed SDR-GB-SAR system obtained by synthesizing $Q = 1, 10, 50$ and 100 NW spectra.

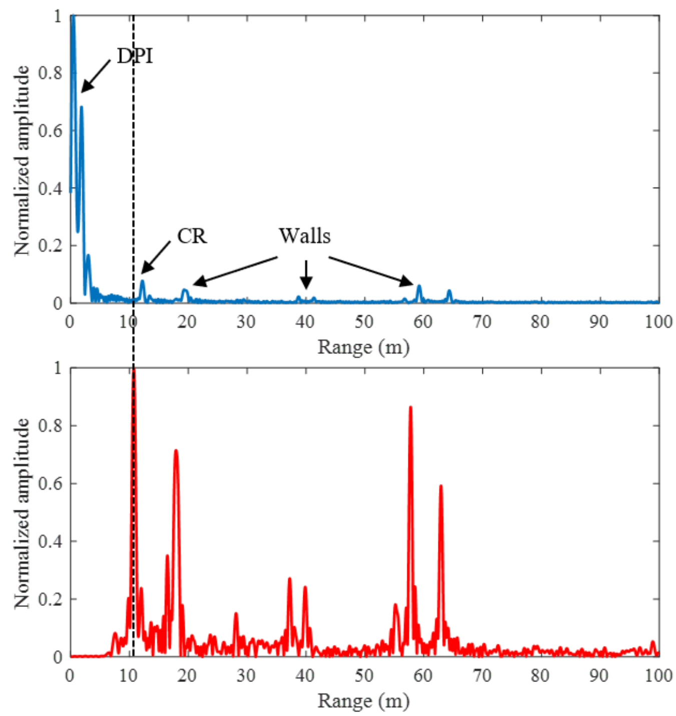

Fig. 9. Range compression results without (top) and with (bottom) DPI suppression and delay-amplitude compensation (T1-R1).

are conducted and the obtained results are averaged. The running time is calculated by the TIC and TOC functions in MATLAB, and, given the ground-truth image $\boldsymbol{\sigma}$ and the image $\widehat{\boldsymbol{\sigma}}$ obtained by each method, the imaging performance of different methods is quantified by the normalized mean squared error (NMSE) in the decibel (dB) unit, defined as

$$NMSE(\widehat{\boldsymbol{\sigma}}, \boldsymbol{\sigma}) = 10\log_{10}[E(||\widehat{\boldsymbol{\sigma}} - \boldsymbol{\sigma}||_2^2/||\boldsymbol{\sigma}||_2^2)] \tag{50}$$

The imaging performance comparison result is shown in the left sub-figure of Fig. 13. It can be seen that: 1) BPA has the highest NMSE; 2) the NMSEs of NUFFT-FISTA are equivalent to those of the original FISTA; 3) the imaging performance of NUFFT-FISTA is worse than the OMP algorithm with 81 iterations (i.e., the target number is exactly known in advance) and is better than the OMP algorithm with 80 iterations (i.e., one target is missed); and 4) the 2D algorithms have much higher NMSEs than their 1D counterparts. The running time comparison result is shown in the right sub-figure of Fig. 13. It can be seen that: 1) the running time of NUFFT-FISTA is almost constant with the changing selected frequency number; and 2) the running time of NUFFT-FISTA is smaller than those of OMP and FISTA when the frequency number becomes larger.

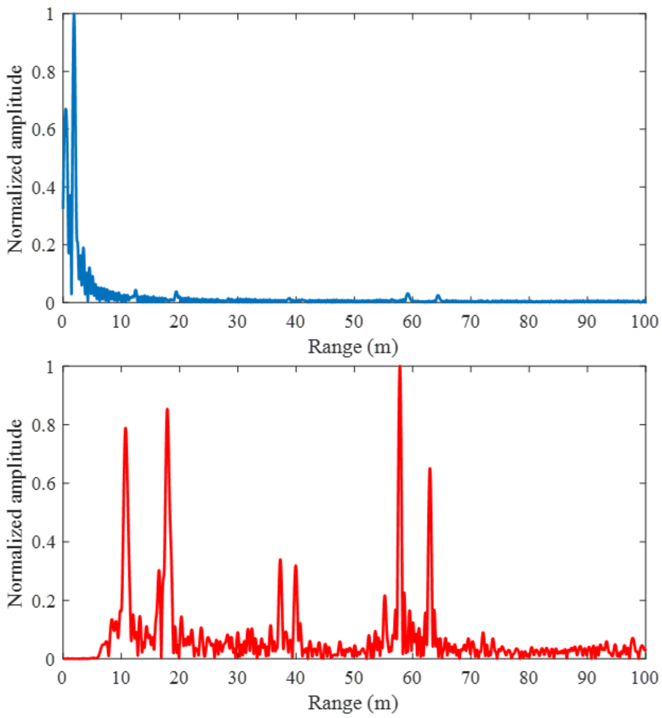

Fig. 10. Range compression results without (top) and with (bottom) DPI suppression and delay-amplitude compensation (T1-R2).

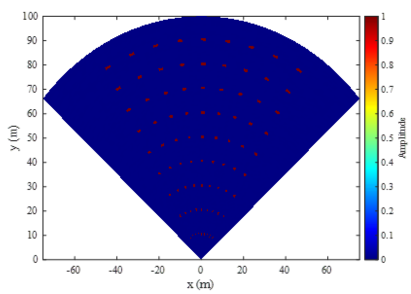

Fig. 11. Simulated targets uniformly distributed in the imaging scene.

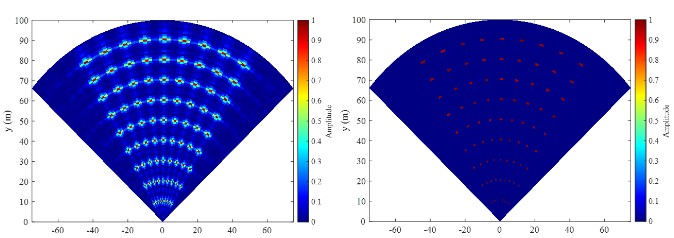

Fig. 12. Imaging results of the simulated targets obtained by BPA (left) and NUFFT-FISTA (right).

Therefore, we can give the following conclusions: 1) compared to BPA, NUFFT-FISTA can achieve better imaging performance; 2) compared to FISTA, NUFFT-FISTA can achieve the same imaging performance with reduced computational complexity when the frequency number is large; 3) compared to OMP, NUFFT-FISTA can obtain the imaging result without knowing the target number in advance and can reduce the running time when the frequency number is large; and 4) as

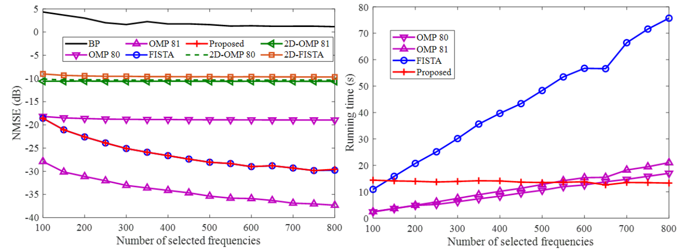

Fig. 13. Imaging performance (left) and running time (right) comparisons of different imaging methods.

the model approximation conditions cannot be satisfied for all the 81 targets, the fast imaging algorithms based on 2D sparse recovery cannot work well in this case, while, on the contrary, no model approximation is needed by NUFFT-FISTA. These conclusions indicate the advantages of NUFFT-FISTA.

Have evaluated the proposed imaging method for GBIR with simulations, we demonstrate its practical performance by experiments in the following. 2D imaging result of the scene shown in the left-top sub-figure of Fig. 5 obtained by the developed SDR-GB-SAR system with NW signal via BPA is shown in Fig. 14, where its overlay above an aerial photography is also illuminated. The system starting carrier frequency is 2400 MHz, carrier frequency number is 400, and synthetic aperture length is about 1.3 m. The transmitting antenna is set at the null radiation direction of the receiving antenna to minimize the influence of DPI. It can be seen that different targets within 100 m range can be well imaged: the house opposite of the balcony facing to the radar system is clearly visible with strong echoes from the metallic structure on the roof, while the strong reflections on the lower part are associated with discontinuities in the roof structure on top of parking boxes acting as dihedral CRs, cars parked close to the radar system also act as strong reflectors.

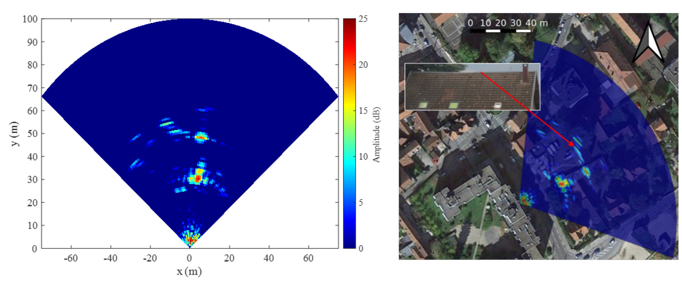

Fig. 14. Experiment target 2D imaging result obtained by the SDR-GB-SAR system (left) and its overlay over the aerial photography of the scene (right). No degree of freedom other than the orientation – defined by the rail parallel to the balcony on which the setup was installed – is available when overlapping the two images.

However, as we can see from Fig. 14, strong sidelobes exist in the obtained image, whose reason is analyzed in the sub-Section D of Section IV. The proposed imaging method NUFFT-FISTA can thus be used to solve this problem, for which, to make it more attractive, only half (randomly selected) of the transmitted carrier frequencies are processed, giving the result shown in Fig. 15. By comparing the images obtained by different methods, it is clear that the proposed imaging method with under-sampled data can achieve better result than BPA with full-sampled and under-sampled data: the resolution is improved and the sidelobe level is much reduced.

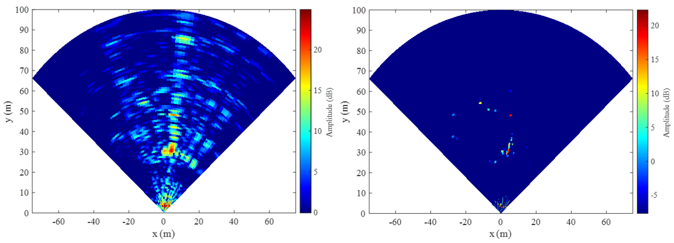

Fig. 15. Experiment target 2D imaging result with half transmitted carrier frequencies obtained by BPA (left) and NUFFT-FISTA (right).

3D imaging result of the scene shown in the left-bottom sub-figure of Fig. 5 obtained by the developed SDR-GB-MIMO radar system with SFCW signal via BPA and NUFFT-FISTA are shown in Fig. 16. The system starting carrier frequency is 4850 MHz, frequency step is 1 MHz, and frequency number is 300. It can be seen that different targets within 100 m range, such as the CR and concrete walls, can be effectively imaged in the 3D space, which is the advantage over the 2D imaging SDR-GB-SAR system as no external digital elevation model is needed for geocoding. Besides, similar to the results shown in Fig. 14, it can also be observed that the proposed imaging method can achieve a higher-quality image than the classical BPA. To more clearly show the performance of the proposed method, a third of carrier frequencies are randomly selected for processing, resulting in the results shown in Fig. 17 with the focus on the three close targets (a CR and two walls). Again, the advantage of the proposed method in sidelobe level and resolution is illustrated with under-sampled data.

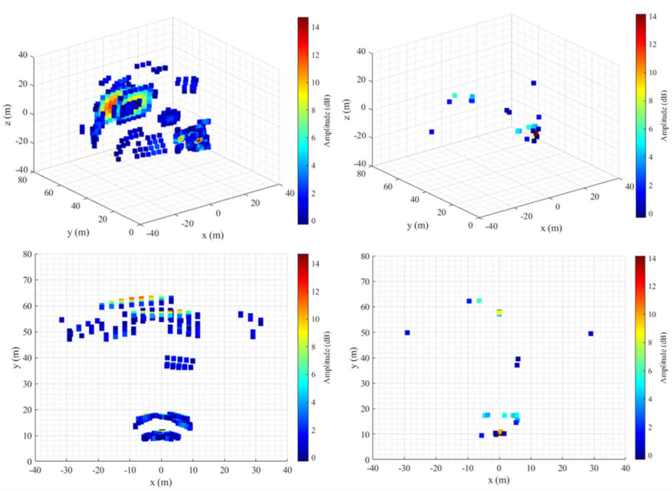

Fig. 16. Experiment target 3D imaging result obtained by BPA (left) and NUFFT-FISTA (right) with all carrier frequencies. The bottom sub-figures are the projection of the top sub-figures on the x-y coordinate.

E. Displacement estimation and analysis

To assess the capacity of the developed system to perform displacement measurement, a trihedral CR with 30 cm-long

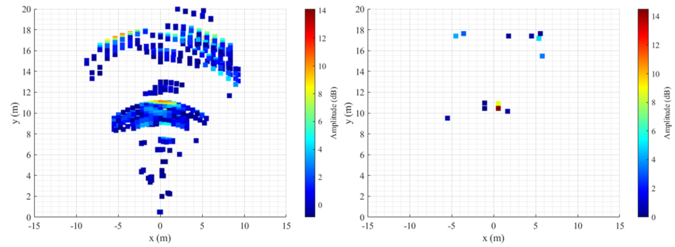

Fig. 17. Experiment target 3D imaging result obtained by BPA (left) and NUFFT-FISTA (right) with a third of carrier frequencies. The 3D images are projected on the x-y coordinate for clarity.

sides was set at the scene shown in the left-top sub-figure of Fig. 5, as shown in Fig. 18, where the distance from the CR to the SDR-GB-SAR system is about 40 m. The dimensions of the CR was selected to match a 2.5 m-diameter sphere, and hence providing a well resolved reflection in front of the various cars parked behind.

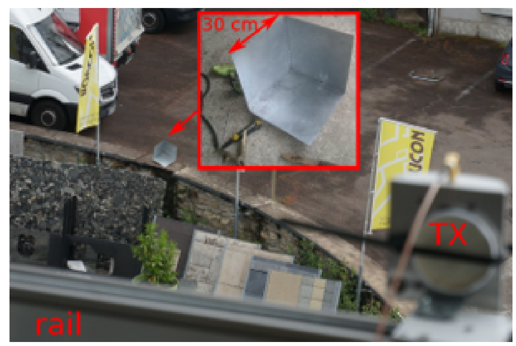

Fig. 18. The CR set in the scene for SDR-GB-SAR displacement estimation.

The imaging result is shown in the left sub-figure of Fig. 19, where the CR is indicated by the rectangle. Besides, to more clearly identify the location of the CR, the amplitude difference between the focused images of the scene with and without the CR is analyzed and shown in the right sub-figure of Fig. 20, demonstrating the appear of a strong target associated with the CR.

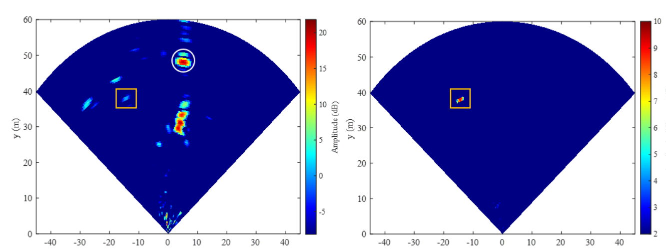

Fig. 19. Imaging result of the scene with the CR (right) and the identification of the CR via amplitude difference calculation (right).

To mimic the displacement, the CR is moved toward the radar system from 1 cm to 9 cm with a step of 1 cm. A full acquisition lasts one hour, half of which is needed to acquire the data and half of which is needed to move the antenna along the rail. Given two adjacent measurements, Fig. 20 shows the coherence image obtained via Eq. (47) with the window size of

8×8 and the displacement map estimated by Eq. (49) for the targets with coherence values higher than 0.8 and normalized amplitudes larger than –30 dB. It can be seen that the man-made targets all have high coherence values, which hints the coherence of the developed SDR-GB-SAR system. Besides, as indicated by the rectangle in the right sub-figure of Fig. 20, the movement of the CR (1 cm) can be accurately estimated.

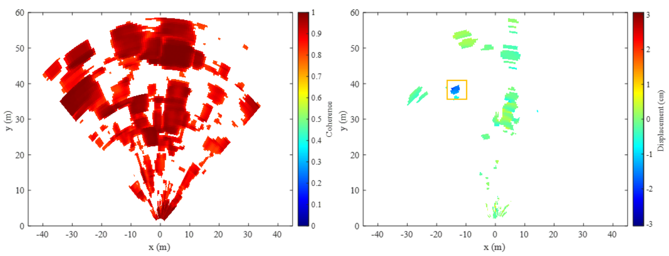

Fig. 20. Coherence image shown with a threshold of 0.8 (left) and target displacement image (left) between two adjacent measurements.

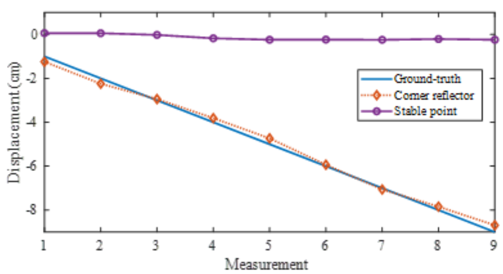

Fig. 21. Accumulated displacements of the CR and the stable house roof during ten-hours measurement.

The accumulated displacements of the CR are then measured, as shown in Fig. 21, where the displacements of a stable point (i.e., the house roof as indicated by the circle in the left sub-figure of Fig. 19, located 48.25 m away from the radar system and assumed to be static during measurement) is also plotted for comparison. Clearly, the target displacements can be accurately estimated: the root mean square errors (RMSEs) of the CR and the stable target are 1.99 mm and 1.86 mm, respectively. In the following, we will explain where the errors come from.

While the variation of the speed of light in air as a function of weather condition is negligible for range measurement, it becomes dramatic for displacement measurement. Actually, a 2-mm error of displacement estimation means measuring 41.5 ppm relative range variations. Optical index of the atmosphere, defining the speed of light variation to its speed in vacuum, is mostly driven by the temperature, pressure and relative moisture [50]. These parameters have been recorded, as found at [51], during the day the measurements for Fig. 21 were collected, as shown in Fig. 22. We can conclude from this figure that, beyond the mean optical index offset of a few hundreds of ppm consistent with the literature [52], a variation of 41.5 ppm can be mostly justified from the moisture level variations over the day. Actually, for long-term displacement monitoring by GBIR, a fixed CR located at a place known to be not moved is classically used as reference for measuring the optical index of air and canceling the impact of weather on the measurement results [2].

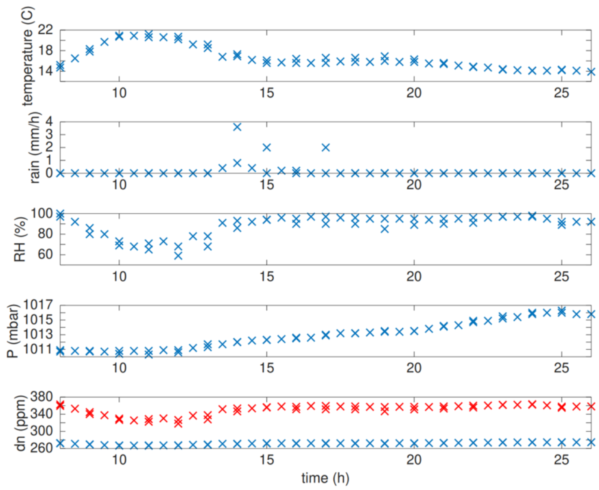

Fig. 22. Weather conditions during the day the displacement measurement was completed, and the resulting optical index variation (bottom) in ppm with respect to the speed of light in vacuum.

F. Implementation based on Wi-Fi signal

At last, we demonstrate the development flexibility of the SDR-GBIR system by replacing the PlutoSDR emitter with a Wi-Fi USB dongle. Actually, since no FPGA firmware needs to be modified, any SDR transmitter and any receiver with at least two coherent channels can be used for SDR-GBIR to enjoy the desired characteristics of different SDR platforms. Compared to PlutoSDR, a Wi-Fi emitter can provide the following two significant benefits: 1) meet radiofrequency emission regulations and combine radar measurement with digital communication, making SDR-GBIR well suited for monitoring displacement in urban conditions with little or no disturbance to existing infrastructures; 2) allow for a bigger carrier frequency step than the PlutoSDR transmission which is limited by the communication bandwidth without the loss of samples since the used Wi-Fi channels are separated by 5 MHz. Actually, the sampling rate is now only limited by the B210 communication over the USB-3 interface as the slower PlutoSDR is no longer the limiting factor, and thus, throughout the experiments with a Wi-Fi emitter, a sampling rate of 5 MHz is used. In our demonstration, despite the near continuous Wi-Fi emission thanks to the software available at [53] that requires a Wi-Fi chipset compatible with the monitoring mode, the successive Wi-Fi packets and associated radiofrequency emissions are observed to be discontinuous. Under such conditions, the reference channel power is monitored and the data collected from the ZeroMQ stream is only saved when this power is above a threshold.

Similar to the frequency-modulated signal and the phase-coded signal, the OFDM approach employed by the Wi-Fi signal is also a popular way to increase the bandwidth in each TR routine, and hence can be applied for bandwidth synthesis in SDR-GBIR to get an increased detection range than the SFCW signal with the same number of carrier frequencies.

In this study, 11 channels of the IEEE 802.11 2.4 GHz Wi-Fi signal are applied to get a range resolution of about 2.7 m. The spectrum of a 2412 MHz Wi-Fi channel is shown in Fig. 23, from which it can be learned that, different from the noise signal spectrum shown in Fig. 7, the OFDW Wi-Fi signal has multiple sub-carriers separated by 312.5 kHz with the missing sub-carrier 0 at the center frequency. In order to avoid the strong spectral feature of the unused sub-carrier 0 at the center frequency of each Wi-Fi channel, the local oscillator of the B210 receiver is offset by 3 MHz with respect to the Wi-Fi transmitter, and thus a 5 MHz bandwidth signal can be collected in each TR routine, as shown in Fig. 24.

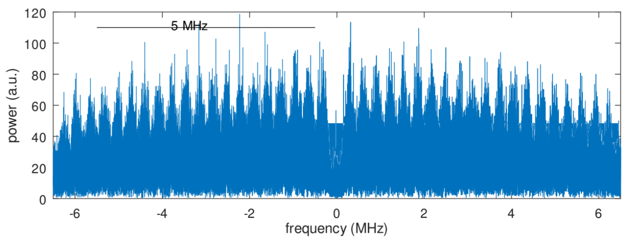

Fig. 23. Spectrum of a Wi-Fi channel emphasizing the OFDM sub-carrier structure separated by 312.5 kHz steps with the missing sub-carrier 0 at center frequency. The indicated 5 MHz spectrum is actually sampled.

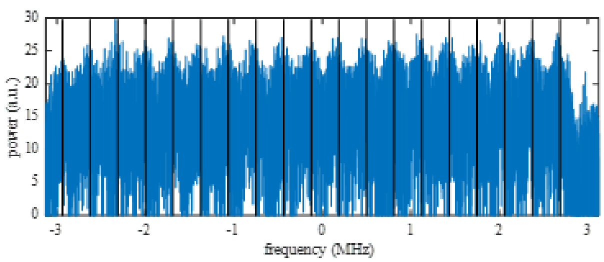

Fig. 24. A 5-MHz wide usable spectrum is collected by offsetting the local oscillators between the B210 receiver and the Wi-Fi transmitter to avoid the missing sub-carrier 0: the Wi-Fi local oscillator is at $2412 + 5(q-1)$ MHz, while the B210 local oscillator is set to 3 MHz below. The vertical lines indicate 19 sub-carriers.

Finally, with the Wi-Fi transmitted signal and a 2.0 m synthetic aperture length, imaging results of the same scene shown in the left-top sub-figure of Fig. 5 are obtained by BPA and NUFFT-FISTA, as shown in Fig. 25. It can be seen that different targets are clearly visible and well consistent with the results obtained by transmitting the NW signal, as shown in Figs. 14 and 15, hence demonstrating the suitability of replacing the PlutoSDR emitter with the Wi-Fi USB dongle for SDR-GBIR development.

VI. Conclusion

We have demonstrated the software defined radio implementation of ground-based interferometric radar by addressing the challenges of system synchronization, bandwidth synthesis, data preprocessing, and target imaging. The developed SDR-GB-SAR and SDR-GB-MIMO radar systems have been validated to work well in practice using the proposed methods for target high-resolution imaging and displacement high-accuracy measurement, enjoying the potentials to reduce the

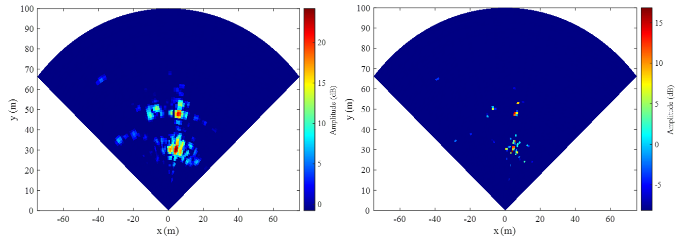

Fig. 25. Imaging results of the same scene as shown in Figs. 14 and 15 by transmitting the Wi-Fi signal, obtained by the BPA (left) and the proposed imaging method (right).

cost and increase the flexibility of current radar systems in the same application field. The setup is furthermore well suited for educational purposes as it only requires widely available and affordable commercial off the shelf hardware, e.g., PlutoSDR or Wi-Fi USB dongle as transmitter, B210 as receiver, and a couple of passive components such as coupler and attenuators in addition to the antennas. All source codes and some datasets resulting from this work are available on the https://github.com/jmfriedt/active_radar Github repository.

Acknowledgements

P. Abbé (FEMTO-ST Time & Frequency, France) assembled the corner reflector displayed in Fig. 18. H. Boeglen (XLim, Poitiers, France) described the Wi-Fi signal structure. This work was partly supported by the Oscillator Instability Measurement Platform (OscillatorIMP) grant from the French National Research Agency as well as the National Natural Science Foundation of China under Grant 62001507 and 61631019.

References

[1] O Monserrat, M Crosetto, and G Luzi, "A review of ground-based SAR interferometry for deformation measurement," *ISPRS Journal of Photogrammetry and Remote Sensing*, vol. 93, pp. 40–48, 2014.

[2] Guido Luzi, Massimiliano Pieraccini, Daniele Mecatti, Linhsia Noferini, Gabriele Guidi, Fabio Moia, and Carlo Atzeni, "Ground-based radar interferometry for landslides monitoring: atmospheric and instrumental decorrelation sources on experimental data," *IEEE transactions on geoscience and remote sensing*, vol. 42, no. 11, pp. 2454–2466, 2004.

[3] Weike Feng, Giovanni Nico, and Motoyuki Sato, "GB-SAR interferometry based on dimension-reduced compressive sensing and multiple measurement vectors model," *IEEE Geoscience and Remote Sensing Letters*, vol. 16, no. 1, pp. 70–74, 2018.

[4] Massimiliano Pieraccini and Lapo Miccinesi, "Ground-based radar interferometry: A bibliographic review," *Remote Sensing*, vol. 11, no. 9, pp. 1029, 2019.

[5] Ashutosh Tiwari, Avadh Bihari Narayan, Ramji Dwivedi, Onkar Dikshit, and B Nagarajan, "Monitoring of landslide activity at the Sirobagarh landslide, Uttarakhand, India, using LiDAR, SAR interferometry and geodetic surveys," *Geocarto International*, vol. 35, no. 5, pp. 535–558, 2020.

[6] Charles Elachi, Tom Bicknell, Rolando L Jordan, and Chialin Wu, "Spaceborne synthetic-aperture imaging radars: Applications, techniques, and technology," *Proceedings of the IEEE*, vol. 70, no. 10, pp. 1174–1209, 1982.

[7] Michele Crosetto, Oriol Monserrat, María Cuevas, and Bruno Crippa, "Spaceborne differential SAR interferometry: Data analysis tools for deformation measurement," *Remote Sensing*, vol. 3, no. 2, pp. 305–318, 2011.

[8] Yuan Gao, Mohammad Tayeb Ghasr, and Reza Zoughi, "Effects of and compensation for translational position error in microwave synthetic aperture radar imaging systems," *IEEE Transactions on Instrumentation and Measurement*, vol. 69, no. 4, pp. 1205–1212, 2019.

[9] Jian Li and Petre Stoica, “MIMO radar with colocated antennas,” *IEEE Signal Processing Magazine*, vol. 24, no. 5, pp. 106–114, 2007.

[10] Dario Tarchi, Nicola Casagli, Sandro Moretti, Davide Leva, and Alois J Sieber, “Monitoring landslide displacements by using ground-based synthetic aperture radar interferometry: Application to the Ruinon landslide in the Italian Alps,” *Journal of Geophysical Research: Solid Earth*, vol. 108, no. B8, 2003.

[11] Sabine Rödelsperger, Gwendolyn Läufer, Carl Gerstenecker, and Matthias Becker, “Monitoring of displacements with ground-based microwave interferometry: IBIS-S and IBIS-L,” *Journal of Applied Geodesy*, vol. 4, no. 1, pp. 41–54, 2010.

[12] Sabine Rödelsperger and Adriano Meta, “Metasensing's FastGBSAR: ground based radar for deformation monitoring,” in *SAR Image Analysis, Modeling, and Techniques XIV*. International Society for Optics and Photonics, 2014, vol. 9243, p. 924318.

[13] Konstantin Lukin, Anatoliy Mogyla, Vladimir Palamarchuk, Pavlo Vyplavin, Evgeniy Kozhan, and Sergey Lukin, “Monitoring of St. Sophia Cathedral interior using Ka-band ground based noise waveform SAR,” in *2009 European Radar Conference (EuRAD)*. IEEE, 2009, pp. 215–217.

[14] Yunhua Luo, Hongjun Song, Robert Wang, Yunkai Deng, Fengjun Zhao, and Zheng Xu, “Arc FMCW SAR and applications in ground monitoring,” *IEEE Transactions on Geoscience and Remote Sensing*, vol. 52, no. 9, pp. 5989–5998, 2014.

[15] Joan Broussolle, Vladimir Kyovtorov, Marco Basso, Guido Ferraro Di Silvi E Castiglione, Jorge Figueiredo Morgado, Raimondo Giuliani, Franco Oliveri, Pier Francesco Sammartino, and Dario Tarchi, “MELISSA, a new class of ground based InSAR system. an example of application in support to the Costa Concordia emergency,” *ISPRS journal of photogrammetry and remote sensing*, vol. 91, pp. 50–58, 2014.

[16] Cheng Hu, Jingyang Wang, Weiming Tian, Tao Zeng, and Rui Wang, “Design and imaging of ground-based multiple-input multiple-output synthetic aperture radar (MIMO SAR) with non-collinear arrays,” *Sensors*, vol. 17, no. 3, pp. 598, 2017.

[17] Alberto Michelini, Francesco Coppi, Alberto Bicci, and Giovanni Alli, “SPARX, a MIMO array for ground-based radar interferometry,” *Sensors*, vol. 19, no. 2, pp. 252, 2019.

[18] Massimiliano Pieraccini and Lapo Miccinesi, “An interferometric MIMO radar for bridge monitoring,” *IEEE Geoscience and Remote Sensing Letters*, vol. 16, no. 9, pp. 1383–1387, 2019.

[19] Weike Feng, Jean-Michel Friedt, Giovanni Nico, and Motoyuki Sato, “3-D ground-based imaging radar based on C-band cross-MIMO array and tensor compressive sensing,” *IEEE Geoscience and Remote Sensing Letters*, vol. 16, no. 10, pp. 1585–1589, 2019.

[20] Sevgi Zubeyde Gurbuz, Hugh D Griffiths, Alexander Charlish, Muralidhar Rangaswamy, Maria Sabrina Greco, and Kristine Bell, “An overview of cognitive radar: Past, present, and future,” *IEEE Aerospace and Electronic Systems Magazine*, vol. 34, no. 12, pp. 6–18, 2019.

[21] Maria S Greco, Fulvio Gini, Pietro Stinco, and Kristine Bell, “Cognitive radars: On the road to reality: Progress thus far and possibilities for the future,” *IEEE Signal Processing Magazine*, vol. 35, no. 4, pp. 112–125, 2018.

[22] Tonmo V Fepeussi, Nicolo Testi, Yang Xu, and Yuanwei Jin, “High-accuracy narrowband software-defined radar using successive multiple-frequency continuous-wave modulation for sensing applications,” *IEEE Transactions on Microwave Theory and Techniques*, vol. 67, no. 9, pp. 3917–3927, 2019.

[23] John Meier, Redmond Kelley, Bradley M Isom, Mark Yeary, and Robert D Palmer, “Leveraging software-defined radio techniques in multichannel digital weather radar receiver design,” *IEEE Transactions on Instrumentation and Measurement*, vol. 61, no. 6, pp. 1571–1582, 2012.

[24] Samuel Prager, Tushar Thrivikraman, Mark S Haynes, John Stang, David Hawkins, and Mahta Moghaddam, “Ultrawideband synthesis for high-range-resolution software-defined radar,” *IEEE Transactions on Instrumentation and Measurement*, vol. 69, no. 6, pp. 3789–3803, 2019.

[25] Weike Feng, Jean-Michel Friedt, Grigory Cherniak, Zhipeng Hu, and Motoyuki Sato, “Direct path interference suppression for short-range passive bistatic synthetic aperture radar imaging based on atomic norm minimisation and vandermonde decomposition,” *IET Radar, Sonar & Navigation*, vol. 13, no. 7, pp. 1171–1179, 2019.

[26] Joseph Landon Garry, Chris J Baker, and Graeme E Smith, “Evaluation of direct signal suppression for passive radar,” *IEEE Transactions on Geoscience and Remote Sensing*, vol. 55, no. 7, pp. 3786–3799, 2017.

[27] Ya-Wei Wang, Guang-Ming Wang, and Bin-Feng Zong, “Directivity improvement of Vivaldi antenna using double-slot structure,” *IEEE Antennas and Wireless Propagation Letters*, vol. 12, pp. 1380–1383, 2013.

[28] Jean-Michel Friedt and Weike Feng, “Software defined radio based synthetic aperture noise and OFDM (Wi-Fi) RADAR mapping,” in *Proceedings of the 10th GNU Radio Conference*, 2020, vol. 5.

[29] Donald R Wehner, “High resolution radar,” *ah*, 1987.

[30] H Schimpf, A Wahlen, and H Essen, “High range resolution by means of synthetic bandwidth generated by frequency-stepped chirps,” *Electronics Letters*, vol. 39, no. 18, pp. 1346–1348, 2003.

[31] MA Temple, KL Sitler, RA Raines, and JA Hughes, “High range resolution (HRR) improvement using synthetic HRR processing and stepped-frequency polyphase coding,” *IEE Proceedings-Radar, Sonar and Navigation*, vol. 151, no. 1, pp. 41–47, 2004.

[32] Inc. Analog Devices, ,” https://github.com/analogdevicesinc/gr-iio/tree/single-param.

[33] Philipp Wojaczek, Fabiola Colone, Diego Cristallini, and Pierfrancesco Lombardo, “Reciprocal-filter-based STAP for passive radar on moving platforms,” *IEEE Transactions on Aerospace and Electronic Systems*, vol. 55, no. 2, pp. 967–988, 2018.

[34] Joaquim Fortuny-Guasch, “A fast and accurate far-field pseudopolar format radar imaging algorithm,” *IEEE transactions on geoscience and remote sensing*, vol. 47, no. 4, pp. 1187–1196, 2009.

[35] Pietro Guccione, Mariantonietta Zonno, Luigi Mascolo, and Giovanni Nico, “Focusing algorithms analysis for ground-based SAR images,” in *2013 IEEE International Geoscience and Remote Sensing Symposium-IGARSS*. IEEE, 2013, pp. 3895–3898.

[36] Dario Tarchi, Franco Oliveri, and Pier Francesco Sammartino, “MIMO radar and ground-based SAR imaging systems: Equivalent approaches for remote sensing,” *IEEE Transactions on Geoscience and Remote Sensing*, vol. 51, no. 1, pp. 425–435, 2012.

[37] Baolong Wu and Lei He, “Multi-layered circular dielectric structure SAR imaging based on compressed sensing for FOD detection in NDT,” *IEEE Transactions on Instrumentation and Measurement*, 2020.

[38] Ingrid Daubechies, Michel Defrise, and Christine De Mol, “An iterative thresholding algorithm for linear inverse problems with a sparsity constraint,” *Communications on Pure and Applied Mathematics: A Journal Issued by the Courant Institute of Mathematical Sciences*, vol. 57, no. 11, pp. 1413–1457, 2004.

[39] Amir Beck and Marc Teboulle, “A fast iterative shrinkage-thresholding algorithm for linear inverse problems,” *SIAM journal on imaging sciences*, vol. 2, no. 1, pp. 183–202, 2009.

[40] Jian Fang, Zongben Xu, Bingchen Zhang, Wen Hong, and Yirong Wu, “Fast compressed sensing SAR imaging based on approximated observation,” *IEEE Journal of Selected Topics in Applied Earth Observations and Remote Sensing*, vol. 7, no. 1, pp. 352–363, 2013.

[41] Hui Bi, Bingchen Zhang, Xiao Xiang Zhu, Chenglong Jiang, and Wen Hong, “Extended chirp scaling-baseband azimuth scaling-based azimuth–range decouple L_1 regularization for TOPS SAR imaging via CAMP,” *IEEE Transactions on Geoscience and Remote Sensing*, vol. 55, no. 7, pp. 3748–3763, 2017.

[42] Leslie Greengard and June-Yub Lee, “Accelerating the nonuniform fast Fourier transform,” *SIAM review*, vol. 46, no. 3, pp. 443–454, 2004.

[43] CMCL, ,” https://cims.nyu.edu/cmcl/nufft/nufft.html.

[44] Alok Dutt and Vladimir Rokhlin, “Fast Fourier transforms for nonequispaced data,” *SIAM Journal on Scientific computing*, vol. 14, no. 6, pp. 1368–1393, 1993.

[45] June-Yub Lee and Leslie Greengard, “The type 3 nonuniform FFT and its applications,” *Journal of Computational Physics*, vol. 206, no. 1, pp. 1 – 5, 2005.

[46] Ramon F Hanssen, *Radar interferometry: data interpretation and error analysis*, vol. 2, Springer Science & Business Media, 2001.

[47] Joel A Tropp and Anna C Gilbert, “Signal recovery from random measurements via orthogonal matching pursuit,” *IEEE Transactions on information theory*, vol. 53, no. 12, pp. 4655–4666, 2007.

[48] David Cohen, Deborah Cohen, Yonina C Eldar, and Alexander M Haimovich, “Summer: Sub-Nyquist MIMO radar,” *IEEE Transactions on Signal Processing*, vol. 66, no. 16, pp. 4315–4330, 2018.

[49] Beiyi Liu, Yu Zhao, Xiaomei Zhu, Shinya Matsushita, and Li Xu, “Sparse detection algorithms based on two-dimensional compressive sensing for sub-nyquist pulse doppler radar systems,” *IEEE Access*, vol. 7, pp. 18649–18661, 2019.

[50] E. K. Smith and S. Weintraub, “The constants in the equation for atmospheric refractive index at radio frequencies,” *Proceedings of the IRE*, vol. 41, no. 8, pp. 1035–1037, 1953.

[51] meteo, ,” https://www.infoclimat.fr/observations-meteo/archives/13/juin/2020/besancon/000P2.html.

[52] Frédéric Fabry, "Meteorological value of ground target measurements by radar," *Journal of Atmospheric and Oceanic Technology*, vol. 21, no. 4, pp. 560–573, 2004.

[53] Bloessl, ," github.com/bastibl/gr-ieee802-11/tree/maint-3.8/utils/packetspammer.